RESEARCH ARTICLE

This article was corrected on 26 JUN 2015. See the end of the full text for details.

Second-moment budgets in cloud topped boundary layers: A large-eddy simulation study

Rieke Heinze[1], Dmitrii Mironov[2], and Siegfried Raasch[1]

[1]Institut für Meteorologie und Klimatologie, Leibniz Universität Hannover, Hannover, Germany, [2]Deutscher Wetterdienst, Offenbach, Germany

Abstract A detailed analysis of second-order moment budgets for cloud topped boundary layers (CTBLs) is performed using high-resolution large-eddy simulation (LES). Two CTBLs are simulated—one with trade wind shallow cumuli, and the other with nocturnal marine stratocumuli. Approximations to the ensemble-mean budgets of the Reynolds-stress components, of the fluxes of two quasi-conservative scalars, and of the scalar variances and covariance are computed by averaging the LES data over horizontal planes and over several hundred time steps. Importantly, the subgrid scale contributions to the budget terms are accounted for. Analysis of the LES-based second-moment budgets reveals, among other things, a paramount importance of the pressure scrambling terms in the Reynolds-stress and scalar-flux budgets. The pressure-strain correlation tends to evenly redistribute kinetic energy between the components, leading to the growth of horizontal-velocity variances at the expense of the vertical-velocity variance which is produced by buoyancy over most of both CTBLs. The pressure gradient-scalar covariances are the major sink terms in the budgets of scalar fluxes. The third-order transport proves to be of secondary importance in the scalar-flux budgets. However, it plays a key role in maintaining budgets of TKE and of the scalar variances and covariance. Results from the second-moment budget analysis suggest that the accuracy of description of the CTBL structure within the second-order closure framework strongly depends on the fidelity of parameterizations of the pressure scrambling terms in the flux budgets and of the third-order transport terms in the variance budgets.

1. Introduction

Shallow clouds, such as stratocumuli and shallow cumuli, are frequently observed over large domains of the Earth. They play a decisive role in determining the thermodynamic state of the atmosphere, e.g., through their effect on the radiation budget of the boundary layer and through the release/consumption of latent heat. The structure and the transport properties of a cloud topped boundary layer (CTBL) is determined by a complex interplay of various physical processes, including kinetic energy production/destruction due to mean-velocity shear and buoyancy, radiative cooling, cloud top entrainment, and large-scale subsidence. A better understanding of physical processes related to shallow clouds and an improved representation of CTBLs in numerical models of atmospheric circulation is crucial for various environmental applications, most notably numerical weather prediction (NWP) and climate modeling.

An immanent feature of CTBLs is the presence of turbulent motions. In NWP and climate models, turbulence must be parameterized because the scales of turbulence are much smaller than the grid spacing typically used. Most (if not all) turbulence parameterization schemes used in NWP and climate models are based on truncated ensemble-mean budget equations for the second-order moments of fluctuating velocity and scalar fields. These schemes range from relatively simple algebraic formulations to quite sophisticated schemes that carry prognostic equations for all second-order moments involved, i.e., for turbulent fluxes of momentum and scalars, velocity and scalar variances, and scalar covariances (see, e.g., *Mironov* [2009], for discussion of second-order closures used in NWP). Hence, good knowledge of the second-moment budgets of fluctuating fields is fundamental for successful use and further development of turbulence parameterization schemes for NWP, climate modeling, and other environmental applications. It is required in particular (i) to access the relative importance of various terms in maintaining the second-moment budgets, small terms can then be discarded and large terms should be appropriately parameterized, (ii) to test various closure

schemes, demonstrate their merits and shortcomings, and, importantly, find their limits of applicability, and (iii) to evaluate disposable parameters of parameterization schemes.

There are numerous observational and large-eddy simulation (LES) studies which focus on the turbulence kinetic energy (TKE) budget in cloud-free convective boundary layers [e.g., *Schmidt and Schumann*, 1989; *Mason*, 1989; *Conzemius and Fedorovich*, 2006; *Pino and de Arellano*, 2008]. Less attention has been paid to the budgets of momentum and scalar fluxes [e.g., *Lenschow et al.*, 1980] and of scalar variances [e.g., *Moeng and Wyngaard*, 1989]. Systematic studies, where all second-moment budgets pertinent to cloud-free convective boundary layers are discussed [e.g., *Deardorff*, 1974a, 1974b; *Mironov et al.*, 2000], are few in number.

In the majority of observational and LES studies of cloudy boundary layers performed to date, consideration has been given to one or the other second-moment budget, most often to the TKE budget [e.g., *Brost et al.*, 1982; *Nicholls and LeMone*, 1982; *Cuijpers and Duynkerke*, 1993; *Brown*, 1999; *Chlond and Wolkau*, 2000; *Grant and Lock*, 2004; *Solomon et al.*, 2011]. Somewhat more detailed studies, where several second-moment budgets in CTBLs are considered, were conducted by *Moeng* [1986] and *Cuijpers et al.* [1996]. The work of *Khairoutdinov and Randall* [2002] is an example of a comprehensive second-moment budget study of the cloudy atmosphere. However, the analysis in *Khairoutdinov and Randall* [2002] is focused on the deep precipitating clouds rather than on shallow nonprecipitating clouds. As to the boundary layers topped by shallow cumulus or stratocumulus clouds, no comprehensive study has been performed so far where all (or most) relevant second-moment budgets are discussed. The present work makes a step forward in this direction. Very high resolution large-eddy simulations of cumulus-topped and stratocumulus-topped boundary-layer flows are conducted. Using LES data, a detailed analysis of the budgets of the Reynolds-stress components (including its trace, i.e., the TKE), of the vertical scalar fluxes, and of the scalar variances is performed.

In what follows, a standard notation is used where t is time, $x_i = (x_1, x_2, x_3)$ are the Cartesian coordinates, g is the acceleration due to gravity, f is the Coriolis parameter, L_v is the latent heat of evaporation, c_p is the specific heat at constant pressure, R_v and R_d are the gas constants for water vapor and for dry air, respectively, $u_i = (u_1, u_2, u_3)$ are the velocity components, p is the perturbation pressure, T is the absolute temperature, θ is the potential temperature, q_v is the (water vapor) specific humidity, and q_l is the specific liquid water content. Reference values of potential temperature and density are denoted by θ_0 and ρ_0, respectively. The virtual potential temperature is defined as $\theta_v = \theta\{1 + [(R_v/R_d) - 1]q_v - q_l\}$. A generic variable s denotes a quasi-conservative scalar that is either the liquid water potential temperature $\theta_l = \theta - (\theta/T)(L_v/c_p)q_l$ or the total water specific humidity $q_t = q_v + q_l$. The Einstein summation convention for repeated indices is used. The Kronecker delta is denoted by δ_{ij}, and the Levi-Civita tensor is denoted by ε_{ijk}. An overbar $\overline{()}$ and a single prime $()'$ denote a resolved-scale (filtered) variable carried by the large-eddy model and a deviation therefrom (i.e., a subfilter-scale fluctuation), respectively. A horizontal mean is denoted by angle brackets $\langle()\rangle$, and a deviation therefrom is denoted by a double prime $()''$. Then, a fluctuating variable a can be represented as $\Phi = \langle\bar{\Phi}\rangle + \bar{\Phi}'' + \Phi'$.

The paper is organized as follows. Section 2 provides a description of the large-eddy model used and of the simulated cases. Section 3 presents the second-moment budget analysis. First (section 3.1), we discuss how approximations to the ensemble-mean second-moment budgets are obtained on the basis of numerical data generated by a large-eddy model. Next (section 3.2), the validity of the approach is examined using LES of the shear-free convective boundary layer with no clouds. Then, the second-moment budgets in CTBLs are discussed in detail (section 3.3), including the budgets of TKE (section 3.3.1) and velocity variances (section 3.3.2), of the vertical momentum and scalar fluxes (sections 3.3.3 and 3.3.4, respectively), and of the scalar variances and covariance (section 3.3.5). Summary and conclusions are presented in section 4.

2. Large-Eddy Model and Simulated Cases

In this study, the parallelized large-eddy model PALM [*Raasch and Schröter*, 2001; *Maronga et al.*, 2015] is utilized. Using the finite difference technique, the model solves the filtered, nonhydrostatic Navier-Stokes equations in the Boussinesq approximation and the filtered transport equations for two quasi-conservative thermodynamic variables, viz., the liquid water potential temperature $\bar{\theta}_l$ and the total water specific

Table 1. Parameters of the Simulated Cases[a]

Case	L_1, L_2 (km)	L_3 (km)	$N_1 \times N_2 \times N_3$	t_{sim} (h)	t_{smpl} (h)	N_{smpl}			
BO	6.4	3.2	$1280 \times 1280 \times 640$	6	3	540			
DY	6.4	1.6	$1280 \times 1280 \times 320$	4	2	360			
FC	4.8	1.9	$960 \times 960 \times 380$	3	2	360			
Case	f (s^{-1})	u_{g1} (m s^{-1})	u_{g2} (m s^{-1})	u_* (m s^{-1})	$H_{\theta 0}$ (K m s^{-1})	H_{q0} (m s^{-1})	Rad. Tend.	Subs. Tend.	Advec. Tend.
BO	1.19×10^{-4}	Prescr.	0.0	0.28	8.00×10^{-3}	5.20×10^{-5}	Prescr.	Prescr.	Prescr.
DY	7.59×10^{-5}	7.0	-5.5	0.25	1.12×10^{-2}	3.82×10^{-5}	Interac.	Prescr.	None
FC	3.76×10^{-5}	0.0	0.0	Interac.	2.40×10^{-1}	None	None	None	None

[a]BO, DY, and FC denote BOMEX, DYCOMS, and case FC, respectively, L_1, L_2, and L_3 are the model domain sizes in x_1, x_2, and x_3 directions, respectively, N_1, N_2, and N_3 are the numbers of grid points in these directions, t_{sim} is the simulation time, t_{smpl} is the sampling time, and N_{smpl} is the number of samples. f is the Coriolis parameter, u_{g1} and u_{g2} are the geostrophic wind components in x_1 and x_2 horizontal directions, respectively, u_* is the surface friction velocity, $H_{\theta 0}$ is the surface flux of liquid water potential temperature, and H_{q0} is the surface flux of total water specific humidity. The abbreviations *rad. tend.*, *subs. tend.*, and *advec. tend.* stand for radiation, subsidence, and advection tendencies, respectively, and *prescr.* and *interac.* stand for prescribed and interactive, respectively. The acceleration due to gravity is $g = 9.81$ m s^{-1} and the reference temperature is $\theta_0 = 300$ K in all three cases.

humidity $\bar{q}_t$. The filtering of the governing equations is carried out implicitly, following the volume-balance approach [*Schumann*, 1975]. The incompressibility of the flow is ensured by solving a Poisson equation for the perturbation pressure, using a predictor-corrector method and a fast Fourier transform. The subgrid-scale (SGS) closure model is based on *Deardorff* [1980], where the SGS fluxes of momentum and scalars are determined through the down-gradient approximation and a prognostic equation for the SGS TKE is carried to determine the SGS eddy diffusivity. The resolved-scale liquid water content $\bar{q}_l$ is calculated by means of a simple saturation adjustment scheme based on *Cuijpers and Duynkerke* [1993], where a grid volume is considered as cloudy when the specific total water content is larger than the saturation specific humidity (all-or-nothing method that does not account for the fractional cloud cover at subgrid scales). Advection of velocity and scalars is computed by a fifth-order scheme based on *Wicker and Skamarock* [2002]. A third-order Runge-Kutta scheme with a variable time step is used for time advance.

The setup of our CTBL simulations is based on two Global Atmospheric System Study (GASS) LES test cases. These are (i) the shallow trade wind cumulus case BOMEX [*Siebesma et al.*, 2003] and (ii) the nocturnal stratocumulus case DYCOMS-II, RF01 [*Stevens et al.*, 2005] (hereinafter referred to as simply DYCOMS). For validation purposes (see section 3.2), a dry shear-free convective boundary layer driven by the surface buoyancy flux is simulated. The setup is based on case FC of *Mironov et al.* [2000, hereinafter M00].

In all simulated cases, periodic boundary conditions in the x_1 and x_2 horizontal directions are applied. The following boundary conditions at the top and the bottom of the model domain are used. At the upper boundary of the domain, vertical gradients of the scalar quantities $\bar{\theta}_l$ and $\bar{q}_t$ and the SGS TKE e are zero, the vertical velocity $\bar{u}_3$ is zero, and the horizontal velocity components are equal to the components of the geostrophic wind, $\bar{u}_1 = u_{g_1}$ and $\bar{u}_2 = u_{g_2}$. At the surface, all three components of the velocity vector are zero. Vertical fluxes of liquid water potential temperature and of total water specific humidity are prescribed, and the x_1 and x_2 components of the surface momentum flux are either evaluated from the surface-layer similarity relations (that are applied locally, i.e., point by point), or computed using prescribed surface friction velocity and the assumption that the momentum flux and the vertical gradient of horizontal velocity are aligned.

We closely follow the setups of BOMEX and DYCOMS described in *Siebesma et al.* [2003] and *Stevens et al.* [2005], respectively. Parameters of the two CTBL simulations are summarized in Table 1. The essential difference between our simulations and the BOMEX and DYCOMS simulations of *Siebesma et al.* [2003] and *Stevens et al.* [2005], respectively, is in the grid spacing. As compared to a rather coarse "original" resolution of BOMEX with the mesh size of 100 m, 100 m, and 40 m in x_1, x_2, and x_3 directions, respectively, and DYCOMS with the mesh size of 35 m, 35 m, and 5 m, respectively, a much finer resolution with a mesh size of 5 m in all directions is used in the present study. Furthermore, the horizontal domain size in the DYCOMS case is nearly doubled as compared to *Stevens et al.* [2005] to become 6.4 km $\times$ 6.4 km. Among other things, a larger domain yields improved estimates of turbulence moments computed on the basis of a large-eddy model output. The BOMEX case was previously simulated with PALM by *Riechelmann et al.* [2012], to validate a Lagrangian cloud model.

The setup of the simulation FC of a dry convective boundary layer driven by the surface buoyancy flux is based on *Mironov et al.* [2000]. Parameters of the simulation are summarized in Table 1. The geostrophic wind components are zero (shear-free convection). The surface temperature flux is $H_{\theta 0} = 2.40 \times 10^{-1}$ K m s^{-1}. The surface temperature is computed by the PALM SGS model on the basis of the Monin-Obukhov surface-layer flux-profile relationships (applied locally). The initial profile of $\bar{\theta}$ has a three-layer structure. A temperature-homogeneous layer with $\bar{\theta} = 300$ K extends from the surface to $x_3 = 1000$ m. It is capped by a 120 m deep strongly stable layer, where the potential-temperature lapse rate is 6.6×10^{-2} K m^{-1}. A stably stratified layer with a lower lapse rate of 3.0×10^{-3} K m^{-1} extends from $x_3 = 1120$ m up to the top of the model domain. The height of the boundary layer z_i is determined as the height where the vertical potential-temperature flux is a minimum. It proves to be equal to $z_i = 1120$ m on the average over the sampling period. The *Deardorff* [1970] convective velocity-scale $w_* = \left(\theta_0^{-1} g z_i H_{\theta 0} \right)^{1/3}$ based on this value of z_i is equal to 2.0 m s^{-1}.

In order to trigger turbulence and reduce the spin-up time, random perturbations are added to the initial velocity and scalar fields in the lower part of the model domain. The turbulence statistics discussed below are the result of averaging over the last 3 h of the simulation in the BOMEX case and over the last 2 h of simulations in the DYCOMS and FC cases. The number of samples is 540 for BOMEX and 360 for DYCOMS and FC.

A quasi-stationary cumulus-topped boundary layer with a four-layer structure is successfully simulated by PALM. Profiles of several turbulence statistics, e.g., the vertical-velocity variance and the fluxes of momentum and of liquid water potential temperature, computed on the basis of PALM output (not shown) are in good agreement with the BOMEX intercomparison results presented in *Siebesma et al.* [2003]. In the stratocumulus DYCOMS case, PALM simulates a well-mixed boundary layer that shows no discernible tendency of decoupling. This is at variance with several members of the DYCOMS ensemble, but in better agreement with observations [see *Stevens et al.*, 2005]. PALM produces some overshooting at the top of the cloud layer. This can be attributed to the use of a nonmonotonic advection scheme that has trouble handling large scalar gradients. Some models from the DYCOMS ensemble reveal similar behavior with respect to the overshooting.

3. Budgets of Second-Order Moments

3.1. Budget Equations

As already mentioned above, most turbulence closure schemes used in NWP and climate models are formulated in terms of ensemble-mean quantities. Then, the ensemble-mean second-moment budgets should be built from the three-dimensional LES fields. Approximations to the ensemble-mean budgets are obtained by first averaging the LES data horizontally and then averaging the resulting profiles over several hundred time steps where the sampling is over the last 3 m and 2 h of the simulations for BOMEX and DYCOMS, respectively.

In order to keep the residuals of the second-moment budgets as small as possible, the SGS contributions to the budgets should be accounted for. These contributions are estimated on the basis of transport equations for the SGS quantities as described in, e.g., M00, *Mironov* [2001] and *Mironov and Sullivan* [2010] but with due regard for the presence of clouds. The procedure is outlined in Appendix A using the scalar-variance budget as an example.

The use of cyclic horizontal boundary conditions results in $\partial \langle \ldots \rangle / \partial x_1 = \partial \langle \ldots \rangle / \partial x_2 = 0$ and $\langle \bar{u}_3 \rangle = 0$. The second-moment budget equations presented below are cast with due regard for these simplifications. Notice, however, that in both BOMEX and DYCOMS tendencies due to large-scale subsidence are added to the prognostic equations for the horizontal velocity components, the liquid water potential temperature and the total water specific humidity. Then, the terms due to large-scale subsidence should also appear in the second-moment budget equations (see Appendix A). Those terms proved to be negligibly small in all second-moment budgets considered in the present paper and are not discussed in what follows.

3.1.1. Reynolds Stress
The budget equation for the Reynolds-stress tensor reads

$$\underbrace{\frac{\partial}{\partial t}\left(\langle\bar{u}_i''\bar{u}_j''\rangle+\langle\tau_{ij}\rangle\right)}_{\mathcal{M}_{ij}} = \underbrace{-\left[\left(\langle\bar{u}_j''\bar{u}_3''\rangle+\langle\tau_{j3}\rangle\right)\frac{\partial\langle\bar{u}_i\rangle}{\partial x_3}+\left(\langle\bar{u}_i''\bar{u}_3''\rangle+\langle\tau_{i3}\rangle\right)\frac{\partial\langle\bar{u}_j\rangle}{\partial x_3}\right]}_{\mathcal{G}_{ij}}$$

$$\underbrace{+\frac{g}{\theta_0}\delta_{i3}\left(\langle\bar{u}_j''\bar{\theta}_v''\rangle+\langle\tau_{vj}\rangle\right)+\frac{g}{\theta_0}\delta_{j3}\left(\langle\bar{u}_i''\bar{\theta}_v''\rangle+\langle\tau_{vi}\rangle\right)}_{\mathcal{B}_{ij}}$$

$$\underbrace{-\left[\epsilon_{ikl}f_k\left(\langle\bar{u}_l''\bar{u}_j''\rangle+\langle\tau_{lj}\rangle\right)+\epsilon_{jkl}f_k\left(\langle\bar{u}_l''\bar{u}_i''\rangle+\langle\tau_{li}\rangle\right)\right]}_{\mathcal{C}_{ij}}$$

$$\underbrace{-\frac{\partial}{\partial x_3}\left(\langle\bar{u}_3''\bar{u}_i''\bar{u}_j''\rangle+\langle\bar{u}_3''\tau_{ij}\rangle+\langle\bar{u}_j''\tau_{i3}\rangle+\langle\bar{u}_i''\tau_{j3}\rangle+\overline{\langle u_3'u_i'u_j'\rangle}\right)}_{\mathcal{T}_{ij}^t}$$
(1)

$$\underbrace{-\frac{1}{\rho_0}\frac{\partial}{\partial x_3}\left(\delta_{j3}\langle\bar{u}_i''\bar{p}''\rangle+\delta_{i3}\langle\bar{u}_j''\bar{p}''\rangle\right)}_{\mathcal{T}_{ij}^p}\underbrace{-\frac{1}{\rho_0}\frac{\partial}{\partial x_3}\left(\delta_{j3}\overline{\langle u_i'p'\rangle}+\delta_{i3}\overline{\langle u_j'p'\rangle}\right)}_{\mathcal{T}_{ij}^{p,sg}}$$

$$\underbrace{+\frac{1}{\rho_0}\left\langle\bar{p}''\left(\frac{\partial\bar{u}_i''}{\partial x_j}+\frac{\partial\bar{u}_j''}{\partial x_i}\right)\right\rangle}_{\Pi_{ij}}+\underbrace{\frac{1}{\rho_0}\overline{\left\langle p'\left(\frac{\partial u_i'}{\partial x_j}+\frac{\partial u_j'}{\partial x_i}\right)\right\rangle}}_{\mathcal{P}_{ij}}\underbrace{-\frac{2}{3}\delta_{ij}\langle\epsilon\rangle}_{\mathcal{D}_{ij}}.$$

The term $\mathcal{M}_{ij}$ on the left-hand side (l.h.s.) of equation (1) is the time-rate-of-change (storage) term, and the terms of the right-hand side (r.h.s.) represent the production/destruction of the Reynolds stress due to mean-velocity shear $\mathcal{G}_{ij}$, production/destruction due to buoyancy $\mathcal{B}_{ij}$, the Coriolis effects $\mathcal{C}_{ij}$, turbulent transport $\mathcal{T}_{ij}^t$, pressure transport $\mathcal{T}_{ij}^p + \mathcal{T}_{ij}^{p,sg}$, pressure redistribution $\Pi_{ij} + \mathcal{P}_{ij}$, and viscous dissipation $\mathcal{D}_{ij}$. The SGS Reynolds stress $\tau_{ij} = \overline{u_i'u_j'}$ is computed by the PALM SGS model. All SGS correlations incorporating virtual potential temperature, viz., $\tau_{vi} = \overline{u_i'\theta_v'}$, $\tau_{v\theta} = \overline{\theta_l'\theta_v'}$, and $\tau_{vq} = \overline{q_t'\theta_v'}$, are expressed in terms of the quasi-conservative quantities θ_l and q_t. The SGS third-order velocity correlations $\overline{u_i'u_j'u_k'}$ as well as the SGS pressure-velocity correlations $\overline{u_i'p'}$ cannot be determined with our large-eddy model. The terms $\partial\langle\overline{u_3'u_i'u_j'}\rangle/\partial x_3$ and $\mathcal{T}_{ij}^{p,sg}$ in (1) are considered as part of the budget residual. These terms are presumably small [e.g., *Deardorff*, 1973] and should not noticeably affect the budget. The SGS contribution to the pressure redistribution (scrambling) term $\mathcal{P}_{ij}$, is estimated on the basis of truncated budget equation for the SGS departure-from-isotropy tensor $\tau_{ij} - \frac{2}{3}e\delta_{ij}$, $e = \frac{1}{2}\tau_{ii}$ being the SGS TKE, assuming a balance between the mean-shear, buoyancy, Coriolis and pressure-scrambling terms at the subgrid scales. The way $\mathcal{P}_{ij}$ is estimated is discussed in detail in Appendix B. It is assumed that viscous dissipation takes place at small scales where, as the Kolmogorov hypothesis states, local isotropy prevails. The Reynolds-stress dissipation is then modeled as an isotropic tensor, as represented by the last term $\mathcal{D}_{ij}$ on the r.h.s. of equation (1) where the TKE dissipation rate ϵ is computed by the SGS model. (Note that it is a common practice in the second-order turbulence closure modeling to either neglect the deviatoric part of the Reynolds-stress dissipation rate tensor, or incorporate it into the so-called slow part of the pressure redistribution term.)

3.1.2. TKE
The transport equation for the TKE $= \frac{1}{2}\langle\bar{u}_i''^2\rangle + \langle e\rangle$ is simply the trace of equation (1) multiplied by 1/2. It reads

$$\underbrace{\frac{\partial}{\partial t}\left(\frac{1}{2}\langle\bar{u}_i''^2\rangle+\langle e\rangle\right)}_{\mathcal{M}_{TKE}} = \underbrace{-\left(\langle\bar{u}_3''\bar{u}_i''\rangle+\langle\tau_{3i}\rangle\right)\frac{\partial\langle\bar{u}_i\rangle}{\partial x_3}}_{\mathcal{G}_{TKE}}+\underbrace{\frac{g}{\theta_0}\left(\langle\bar{u}_3''\bar{\theta}_v''\rangle+\langle\tau_{v3}\rangle\right)}_{\mathcal{B}_{TKE}}$$

$$\underbrace{-\frac{\partial}{\partial x_3}\left[\frac{1}{2}\langle\bar{u}_3''\bar{u}_i''^2\rangle+\langle\bar{u}_3''e''\rangle+\langle\bar{u}_i''\tau_{i3}\rangle+\frac{1}{2}\overline{\langle u_3'u_i'^2\rangle}\right]}_{\mathcal{T}_{TKE}^t}$$
(2)

$$\underbrace{-\frac{1}{\rho_0}\frac{\partial}{\partial x_3}\left[\langle\bar{u}_3''\bar{p}''\rangle+\overline{\langle u_3'p'\rangle}\right]}_{\mathcal{T}_{TKE}^p}\underbrace{-\langle\epsilon\rangle}_{\mathcal{D}_{TKE}}.$$

The TKE time-rate-of-change $\mathcal{M}_{\text{TKE}}$ is due to shear production/destruction $\mathcal{G}_{\text{TKE}}$, buoyancy production/destruction $\mathcal{B}_{\text{TKE}}$, turbulent transport $\mathcal{T}^{\text{t}}_{\text{TKE}}$, pressure transport $\mathcal{T}^{\text{p}}_{\text{TKE}}$, and dissipation $\mathcal{D}_{\text{TKE}}$. Neither the Coriolis terms, nor the pressure scrambling terms appear in the TKE budget. Those terms do not produce kinetic energy but only act to redistribute energy between the components. Within the SGS model used by PALM, the sum of the SGS transport terms $\frac{1}{2}\overline{u'_3 u'^2_i} + \rho_0^{-1}\overline{u'_3 p'}$ is parameterized through the down-gradient diffusion approximation. It is, therefore, not possible to distinguish between the third-order transport and the pressure transport of the SGS TKE. In the subsequent analysis, the entire SGS transport term $\frac{1}{2}\overline{u'_3 u'^2_i} + \rho_0^{-1}\overline{u'_3 p'}$ is considered, albeit somewhat arbitrarily, as part of $\mathcal{T}^{\text{p}}_{\text{TKE}}$.

3.1.3. Scalar Fluxes

The scalar-flux budget equation is presented in terms of a generic variable s that denotes either the liquid water potential temperature θ_{l}, or the total water specific humidity q_{t}. The budget reads

$$
\underbrace{\frac{\partial}{\partial t}\left(\langle \overline{u''_i s''}\rangle + \langle \tau_{si}\rangle\right)}_{\mathcal{M}_{si}} = \underbrace{-\left(\langle \overline{u''_3 u''_i}\rangle + \langle \tau_{i3}\rangle\right)\frac{\partial \langle \overline{s}\rangle}{\partial x_3}}_{\mathcal{G}^s_{si}} \underbrace{- \left(\langle \overline{u''_3 s''}\rangle + \langle \tau_{s3}\rangle\right)\frac{\partial \langle \overline{u}_i\rangle}{\partial x_3}}_{\mathcal{G}^u_{si}} + \underbrace{\frac{g}{\theta_0}\delta_{i3}\left(\langle \overline{s'' \theta''_v}\rangle + \langle \tau_{vs}\rangle\right)}_{\mathcal{B}_{si}}
$$

$$
\underbrace{-\epsilon_{ijk}f_j\left(\langle \overline{u''_k s''}\rangle + \langle \tau_{sk}\rangle\right)}_{\mathcal{C}_{si}} \underbrace{- \frac{\partial}{\partial x_3}\left[\langle \overline{u''_3 u''_i s''}\rangle + \langle \overline{u''_3 \tau_{si}}\rangle + \langle \overline{u''_i \tau_{s3}}\rangle + \langle \overline{s'' \tau_{i3}}\rangle + \langle \overline{u'_3 u'_i s'}\rangle\right]}_{\mathcal{T}_{si}} \tag{3}
$$

$$
\underbrace{-\frac{1}{\rho_0}\left\langle \overline{s''\frac{\partial \overline{p}''}{\partial x_i}}\right\rangle}_{\Pi_{si}} \underbrace{- \frac{1}{\rho_0}\left\langle \overline{s'\frac{\partial p'}{\partial x_i}}\right\rangle}_{\mathcal{P}_{si}} + \underbrace{\langle \overline{u''_i \overline{Q}'_s}\rangle}_{\mathcal{Q}_{si}}.
$$

The scalar-flux time-rate-of-change $\mathcal{M}_{si}$ is due to the production/destruction by mean scalar gradient $\mathcal{G}^s_{si}$ and mean-velocity gradient $\mathcal{G}^u_{si}$, buoyancy production/destruction $\mathcal{B}_{si}$, Coriolis effects $\mathcal{C}_{si}$, turbulent transport $\mathcal{T}_{si}$, pressure gradient-scalar covariance $\Pi_{si} + \mathcal{P}_{si}$, and the scalar source term $\mathcal{Q}_{si}$. Formally speaking, equation (3) also contains the SGS source terms $\langle \overline{u'_i Q'_s}\rangle$. However, the SGS source terms are not included into a rather simple SGS model used by PALM. The only resolved-scale source term that appears in the budget equations for the scalar fluxes is the source term $\mathcal{Q}_{\theta i}$ due to horizontally inhomogeneous radiative forcing in the DYCOMS stratocumulus-topped boundary-layer case. The term $\mathcal{Q}_{\theta i}$ proves to be negligibly small throughout the model domain, including the cloud layer, and is not considered in what follows. The SGS scalar flux $\tau_{si} = \overline{u'_i s'}$ is computed by the SGS model. The SGS triple correlation $\overline{u'_i u'_j s'}$ cannot be determined with our large-eddy model. The term $\partial\langle \overline{u'_3 u'_i s'}\rangle/\partial x_3$ in (3) is considered as part of the budget residual. The SGS scalar-virtual potential temperature covariance $\tau_{vs} = \overline{s' \theta'_v}$ is not computed by the SGS model. It is expressed in terms of the quasi-conservative quantities θ_{l} and q_{t}, and the (co)variances $\tau_{\theta s} = \overline{s' \theta'_{\text{l}}}$ and $\tau_{qs} = \overline{s' q'_{\text{t}}}$ are then estimated on the basis of truncated SGS equations assuming a steady state balance between the mean-gradient production and dissipation at the subgrid scales. The SGS contribution to the pressure gradient-scalar covariance $\mathcal{P}_{s3}$ is estimated, analogously to $\mathcal{P}_{ij}$, on the basis of a truncated SGS scalar-flux budget, assuming a steady state balance between the mean-gradient, buoyancy, Coriolis and pressure gradient-scalar covariance terms at the subgrid scales (see Appendix B for details). *Khanna* [1998], M00, and *Mironov* [2001] showed that $\mathcal{P}_{si}$ should be accounted for in the scalar-flux budget to obtain a small budget residual.

3.1.4. Scalar Variances and Covariance

As in the section 3.1.3, a generic variable s is used. The budget equation for the scalar variance reads

$$
\underbrace{\frac{1}{2}\frac{\partial}{\partial t}\left(\langle \overline{s''^2}\rangle + \langle \zeta\rangle\right)}_{\mathcal{M}_{ss}} = \underbrace{-\left(\langle \overline{u''_3 s''}\rangle + \langle \tau_{s3}\rangle\right)\frac{\partial \langle \overline{s}\rangle}{\partial x_3}}_{\mathcal{G}_{ss}} \underbrace{- \frac{1}{2}\frac{\partial}{\partial x_3}\left[\langle \overline{u''_3 s''^2}\rangle + \langle \overline{u''_3 \zeta''}\rangle + 2\langle \overline{s'' \tau_{s3}}\rangle + \langle \overline{u'_3 s'^2}\rangle\right]}_{\mathcal{T}_{ss}} \tag{4}
$$

$$
\underbrace{-\langle \epsilon_s\rangle}_{\mathcal{D}_{ss}} + \underbrace{\langle \overline{s'' \overline{Q}''_s}\rangle}_{\mathcal{Q}_{ss}}.
$$

The scalar-variance time-rate-of-change $\mathcal{M}_{ss}$ is due to the mean-gradient production/destruction $\mathcal{G}_{ss}$, turbulent transport $\mathcal{T}_{ss}$, dissipation $\mathcal{D}_{ss}$, and the source term $\mathcal{Q}_{ss}$. The only contribution to $\mathcal{Q}_{ss}$ is due to horizontally inhomogeneous radiative forcing in the DYCOMS simulation. This term is rather small in comparison to

the other budget terms (as is the case in the scalar-flux budgets) and is not considered in what follows. The SGS contribution $\langle s'Q_s'\rangle$ to the source term should formally appear on the r.h.s. of equation (4). The SGS source terms are not accounted for within the PALM SGS model, however. A detailed derivation of equation (4) is given in Appendix A.

The budget equation for the covariance of liquid water potential temperature and total water specific humidity, which is discussed here for the first time for CTBLs, reads

$$\underbrace{\frac{\partial}{\partial t}\left(\langle \bar{q}_t''\bar{\theta}_l''\rangle + \langle \tau_{\theta q}\rangle\right)}_{\mathcal{M}_{q\theta}} = \underbrace{-\left(\langle \bar{u}_3''\bar{\theta}_l''\rangle + \langle \tau_{\theta 3}\rangle\right)\frac{\partial \langle \bar{q}_t\rangle}{\partial x_3}}_{\mathcal{G}_{q\theta}^q} \underbrace{-\left(\langle \bar{u}_3''\bar{q}_t''\rangle + \langle \tau_{q3}\rangle\right)\frac{\partial \langle \bar{\theta}_l\rangle}{\partial x_3}}_{\mathcal{G}_{q\theta}^\theta}$$

$$\underbrace{-\frac{\partial}{\partial x_3}\left[\langle \bar{u}_3''\bar{q}_t''\bar{\theta}_l''\rangle + \langle \bar{u}_3''\tau_{\theta q}\rangle + \langle \bar{q}_t''\tau_{\theta 3}\rangle + \langle \bar{\theta}_l''\tau_{q3}\rangle + \overline{\langle u_3'q_t'\theta_l'\rangle}\right]}_{\mathcal{T}_{q\theta}} \qquad (5)$$

$$\underbrace{-2\langle \epsilon_{\theta q}\rangle}_{\mathcal{D}_{q\theta}} \underbrace{+\langle \bar{q}_t''\bar{Q}_\theta''\rangle + \langle \bar{\theta}_l''\bar{Q}_q''\rangle}_{\mathcal{Q}_{q\theta}}.$$

The covariance budget equation includes the time-rate-of-change term $\mathcal{M}_{q\theta}$, the production/destruction terms due to mean gradient of total water specific humidity, $\mathcal{G}_{q\theta}^q$, and mean gradient of liquid water potential temperature, $\mathcal{G}_{q\theta}^\theta$, the turbulent transport term $\mathcal{T}_{q\theta}$, the dissipation (molecular destruction) term $\mathcal{D}_{q\theta}$, and the source term $\mathcal{Q}_{q\theta}$. As in equations (3) and (4), the SGS source terms $\langle \overline{q_t'Q_\theta'}\rangle$ and $\langle \overline{\theta_l'Q_q'}\rangle$ should formally appear in equation (5). Recall that these source terms are not accounted for within the PALM SGS model. There is no source/sink of the total water specific humidity if precipitation is not considered, and the source/sink of the liquid water potential temperature due to horizontally inhomogeneous radiative forcing in the DYCOMS simulation is very small. Hence, $\mathcal{Q}_{q\theta}$ is not considered in what follows. The SGS scalar variances $\zeta = \overline{s'^2}$ and scalar covariance $\tau_{\theta q} = \overline{q_t'\theta_l'}$ are not computed by the PALM SGS model. They are estimated on the basis of the SGS scalar (co)variance equations, assuming local isotropy and local balance between the mean-gradient production and the dissipation (molecular destruction) at the subgrid scales. Using a parameterization for the scalar dissipation rate ϵ_s after Deardorff [1973, equation (3.4)], we obtain $\zeta = 5\tau_{si}^2/e$ and $\tau_{\theta q} = 5\tau_{\theta i}\tau_{qi}/e$. The numerical value of the coefficient follows from consideration of the inertial subrange temperature spectrum [*Moeng and Wyngaard*, 1988; see also M00]. The SGS triple correlations $\overline{u_i's'^2}$ and $\overline{u_i'q_t'\theta_l'}$ cannot be computed with our large-eddy model. The terms $\partial \langle \overline{u_3's'^2}\rangle/\partial x_3$ and $\partial \langle \overline{u_3'q_t'\theta_l'}\rangle/\partial x_3$ in (4) and (5), respectively, are considered as part of the residual. The dissipation rates of the scalar variances and covariance are estimated as $\epsilon_s = K_h(\partial \bar{s}/\partial x_i)^2$ and $\epsilon_{\theta q} = K_h(\partial \bar{\theta}_l/\partial x_i)(\partial \bar{q}_t/\partial x_i)$ (Appendix A) [see also *Peltier and Wyngaard*, 1995].

Table 2 summarizes the SGS budget terms that cannot be computed with the PALM SGS model and are neglected. Those terms are treated as part of the residual of the respective budget.

3.2. Fidelity of LES-Based Second-Moment Budgets
The budgets of the TKE, of the temperature variance and of the vertical temperature flux from the dry shear-free convective boundary-layer simulation FC are compared with the respective budgets presented by M00. The present results are in good agreement with the M00 results as to all terms in the second-moment budgets except for the TKE dissipation rate $\mathcal{D}_{TKE}$. The residuals of the temperature-variance and the temperature-flux budgets (not shown) are negligibly small between $0.2z_i$ and $0.9z_i$, z_i being the height of the boundary layer. In the interfacial layer capping the convectively mixed layer, the residuals are not entirely negligible but are much smaller than the leading-order terms. In the vicinity of the underlying surface, where LES is known to be less reliable, the budget residuals are larger. Note that, as distinct from PALM, the large-eddy model applied by M00 uses a pseudospectral method to evaluate the horizontal derivatives.

Table 2. Neglected SGS Terms in the Second-Moment Budget Equations

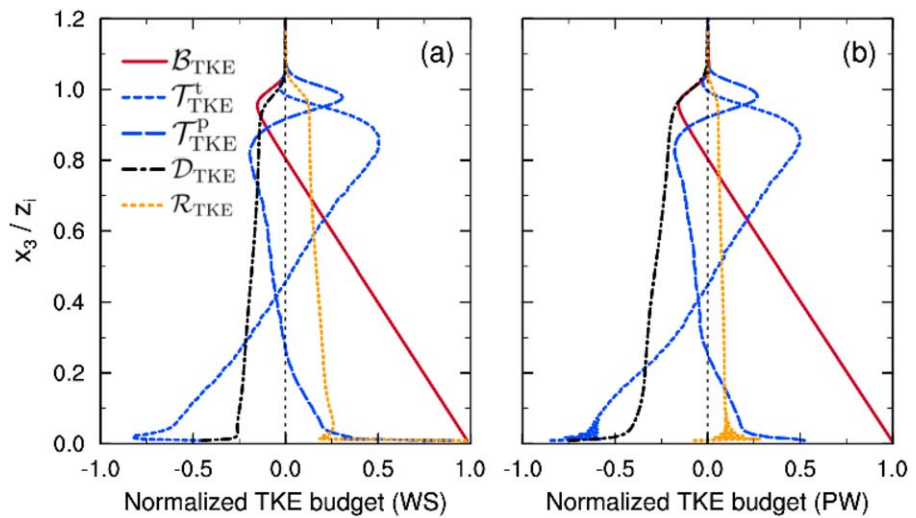| Budget	SGS Triple Correlation	SGS Source Term	SGS Pressure Term
Reynolds stress	$\overline{u_3'u_i'u_j'}$		$\overline{u_i'p'}$
Scalar fluxes	$\overline{u_i'u_j's'}$	$\overline{u_i'Q_s'}$	
Scalar variances	$\overline{u_i's'^2}$	$\overline{s'Q_s'}$	
Scalar covariance	$\overline{u_i'q_t'\theta_l'}$	$\overline{\theta_l'Q_q'}, \overline{q_t'Q_\theta'}$	

Figure 1. Vertical profiles of terms in the TKE budget, equation (2), from simulation FC using (a) the fifth-order advection scheme of *Wicker and Skamarock* [2002] and (b) the second-order advection scheme of *Piacsek and Williams* [1970]. Solid red lines represent buoyancy production/destruction $\mathcal{B}_{TKE}$, blue short-dashed—turbulent transport $\mathcal{T}^{t}_{TKE}$, blue long-dashed—pressure transport $\mathcal{T}^{p}_{TKE}$, black dot-dashed—dissipation $\mathcal{D}_{TKE}$, and orange dotted—the budget residual $\mathcal{R}_{TKE}$. The shear production term $\mathcal{G}_{TKE}$ is zero in the FC case. The storage term $\mathcal{M}_{TKE}$ is very small and is not plotted. The budget terms are normalized with $z_i^{-1} w_*^3$, where $z_i = 1120$ m is the boundary-layer depth and $w_* = 2.0$ ms^{-1} is the convective velocity scale. These estimates of z_i and w_* are obtained by means of averaging over the last 2 h of the simulation.

Since the results of spectral models are generally more accurate than those of finite-difference models [*Glendening and Haack*, 2001], slightly larger residuals of the budgets may be expected in the PALM simulations.

The TKE budget from the simulation FC, performed with the PALM default fifth-order advection scheme based on *Wicker and Skamarock* [2002, hereinafter WS], is shown in Figure 1a. As seen from the figure, the TKE budget residual (the sum of all budget terms), $\mathcal{R}_{TKE} = \mathcal{B}_{TKE} + \mathcal{T}^{t}_{TKE} + \mathcal{T}^{p}_{TKE} + \mathcal{D}_{TKE} - \mathcal{M}_{TKE}$, is almost a mirror image of the TKE dissipation rate and is large. The TKE dissipation rate proves to be the only term in the second-moment budgets that differs significantly in magnitude (but, curiously, not in shape of the profile) from the M00 estimate (see their Figure 11a). A strong underestimation of dissipation in the PALM simulation does not make it possible to close the TKE budget to a good order. It should be mentioned that in the present analysis profiles are first averaged over time and then normalized with the time-mean Deardorff convective scales z_i and w_*. In M00, profiles are normalized with the values of z_i and w_* pertinent to individual profiles prior to time averaging. Since z_i increases only slightly over the simulation period in the case FC, the difference in the normalization and time averaging procedure does not noticeably affect the results, however.

In order to understand what causes trouble with the TKE dissipation rate, an additional simulation was performed using a second-order advection scheme based on *Piacsek and Williams* [1970, hereinafter PW]. The result is shown in Figure 1b. As compared to the simulation with the PALM default WS-scheme (Figure 1a), the dissipation rate is nearly doubled and the TKE budget residual is nearly halved, whereas the other budget terms reveal practically no dependence on the advection scheme. The dependence of dissipation on the advection scheme can be attributed to the effect of numerical diffusion. The fifth-order WS-scheme has favorable dispersion properties but is rather diffusive, leading to smoothed velocity and scalar fields at scales close to the cutoff wave number. This results in a reduced energy in the high wave number part of the spectrum [see e.g., *Morinishi et al.*, 1998] and a reduced scale-interaction term $\langle \bar{u}_i'' \partial \tau_{ij}'' / \partial x_j \rangle$ that describes the transfer of kinetic energy from the resolved scale part of the energy spectrum to the subgrid scale part of the spectrum where the TKE eventually dissipates (see Appendix A for the discussion of the scale-interaction term). At high spatial resolution, the principal balance in the SGS TKE equation is between the spectral transfer of energy from the resolved to the subgrid scales and the viscous dissipation, the other terms being (much) smaller. Then, underestimation of the scale-interaction term immediately leads to
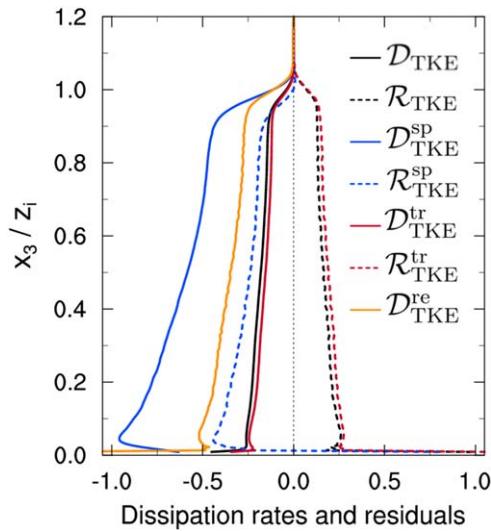
Figure 2. Vertical profiles of the various estimates of the TKE dissipation rate $\mathcal{D}$ (solid curves) and the respective TKE budget residuals $\mathcal{R}$ (dashed curves) from the simulation FC with the *Wicker and Skamarock* [2002] advection scheme. Black lines show the dissipation rate $\mathcal{D}_{TKE}$ and the residual $\mathcal{R}_{TKE}$ computed by the PALM SGS model, blue lines show $\mathcal{D}_{TKE}^{sp}$ and $\mathcal{R}_{TKE}^{sp}$ estimated from the energy spectra, and red lines show $\mathcal{D}_{TKE}^{tr}$ and $\mathcal{R}_{TKE}^{tr}$ estimated from the resolved TKE budget. Orange solid line shows the dissipation rate $\mathcal{D}_{TKE}^{re}$ estimated as the sum of all TKE budget terms except for dissipation (the respective budget residual is zero by definition). Profiles are normalized with $z_i^{-1} w_*^3$ as in Figure 1.

underestimation of the TKE dissipation rate. The use of the less diffusive second-order PW-scheme yields an improved estimate of the TKE dissipation rate and a smaller TKE budget residual. The residual is still significant, however. This can be attributed to numerical errors of the time stepping scheme and/or spatial discretization errors, which sometimes appear to be larger than the SGS flux divergence terms, especially in finite difference models [e.g., *Ghosal*, 1996].

Apart from the use of the SGS TKE equation, there are other methods to estimate the TKE dissipation rate. One possibility is to make use of the scale-interaction term in the resolved-scale TKE budget [e.g., *Moeng*, 1986]. Then, the TKE dissipation rate is estimated as

$$\mathcal{D}_{TKE}^{tr} = \left\langle \bar{u}_i'' \frac{\partial \tau_{ij}''}{\partial x_j} \right\rangle. \tag{6}$$

Equation (6) amounts to the assumption that the transfer of energy from the resolved to the subgrid scales is (exactly) balanced by viscous dissi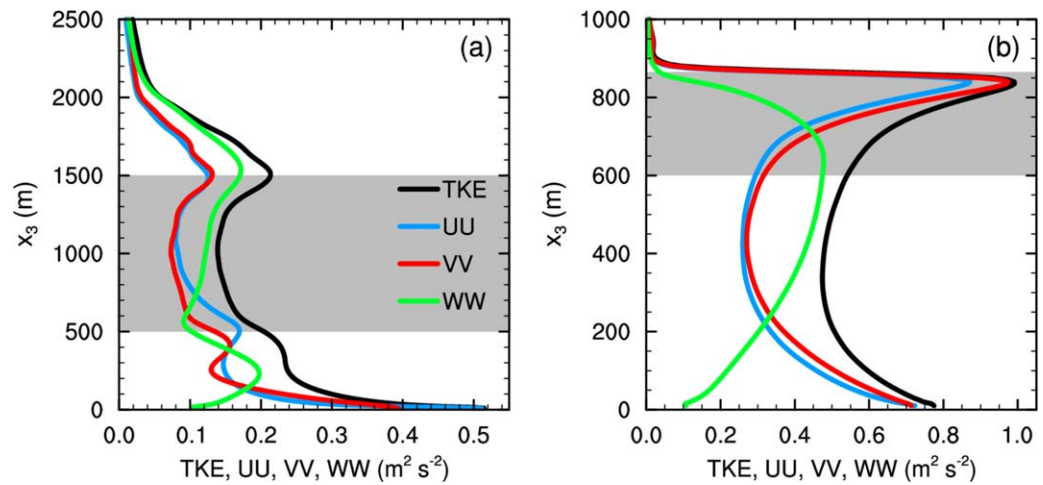pation (see above). The dissipation rate can also be estimated on the basis of the energy spectra [e.g., *Cuijpers et al.*, 1996]. The respective dissipation rate is denoted by $\mathcal{D}_{TKE}^{sp}$ and is computed as described in *Maronga et al.* [2013]. One more possibility to estimate the TKE dissipation rate is to take it to be equal to the sum of all other TKE budget terms, that is

$$\mathcal{D}_{TKE}^{re} = -\mathcal{G}_{TKE} - \mathcal{B}_{TKE} - \mathcal{T}_{TKE}^{t} - \mathcal{T}_{TKE}^{p} + \mathcal{M}_{TKE}. \tag{7}$$

Using this method (that can be referred to as the "residual method"), all the uncertainties associated with the other terms in the TKE budget are lumped on $\mathcal{D}_{TKE}^{re}$ [e.g., *Stull*, 1988, p. 431].

Figure 2 shows the dissipation rate estimates $\mathcal{D}_{TKE}$, $\mathcal{D}_{TKE}^{sp}$, $\mathcal{D}_{TKE}^{tr}$, and $\mathcal{D}_{TKE}^{re}$ along with the respective residuals of the TKE budget from the simulation FC. The estimates $\mathcal{D}_{TKE}$ (black line) and $\mathcal{D}_{TKE}^{tr}$ (red line) proved to be very similar, corroborating our finding (see above) that the use of the WS-scheme causes high numerical diffusion and results in an underestimation of the energy transfer from the resolved to the subgrid scales. The estimate $\mathcal{D}_{TKE}^{sp}$ based on the energy spectra (blue line) proves to be about 3 times larger than $\mathcal{D}_{TKE}$. The respective residual $\mathcal{R}_{TKE}^{sp}$ is negative and large, indicating that the spectral method (strongly) overestimates the TKE dissipation rate. This is not surprising, however, considering spurious effects due to high numerical diffusion, i.e., reduced energy at small scales and the associated too rapid fall-off of the energy spectrum. *Maronga et al.* [2013] also found that the fall-off of the spectrum in their simulations is intensified by numerical diffusion. The estimate $\mathcal{D}_{TKE}^{re}$ (orange line) obtained with the residual method agrees well (both in terms of the magnitude and the shape of the vertical profile) with the TKE dissipation rate computed by M00. As $\mathcal{D}_{TKE}^{re}$ is the only estimate of the TKE dissipation rate that is in good agreement with the results from the "reference" simulation of M00, $\mathcal{D}_{TKE}^{re}$ is used instead of $\mathcal{D}_{TKE}$ in the subsequent analysis of the TKE and velocity variance budgets.

3.3. Analysis of LES Data
3.3.1. TKE
Vertical profiles of TKE are shown in Figure 3. In the cumulus-topped boundary layer, Figure 3a, the TKE has a maximum near the surface where it is produced due to a large mean-velocity shear (and, to a lesser degree, by buoyancy), it decreases up to $z \approx 1000$ m, and has another peak at the top of the conditionally unstable layer ($x_3 \approx 1500$ m) where the TKE production is largely due to release of latent heat.

Figure 3. Vertical profiles of TKE $= \frac{1}{2}\langle \bar{u}_i''^2 \rangle + \langle e \rangle$, horizontal-velocity variances UU $= \langle \bar{u}_1''^2 \rangle + \langle \tau_{11} \rangle$ and VV $= \langle \bar{u}_2''^2 \rangle + \langle \tau_{22} \rangle$, and vertical-velocity variance WW $= \langle \bar{u}_3''^2 \rangle + \langle \tau_{33} \rangle$ for (a) BOMEX and (b) DYCOMS. The profiles are obtained by means of averaging over the last 3 h of simulation for BOMEX and over the last 2 h of simulation for DYCOMS. The gray shading indicates the cloud layer.

The profile of TKE in the stratocumulus-topped boundary layer, Figure 3b, also shows large values near the surface. A peak near the top of the stratocumulus layer is even more pronounced than in the cumulus case.

Vertical profiles of terms in the TKE budget are shown in Figure 4. In both CTBLs, the TKE production due to mean-velocity shear $\mathcal{G}_{TKE}$ is large near the surface, where it is the leading-order term in the TKE budget, and is small aloft. In the BOMEX case (Figure 4a), however, there is also substantial TKE production at the bottom of the cloud layer due to directional shear (the wind turns quickly toward the geostrophic wind).

In contrast to the mean-velocity shear term, the buoyancy term $\mathcal{B}_{TKE}$ is important over the entire boundary layer. In both CTBLs, $\mathcal{B}_{TKE}$ decreases linearly with height from the surface to the top of the subcloud layer. In the BOMEX case, Figure 4a, the profile of $\mathcal{B}_{TKE}$ in the subcloud layer is very similar to the buoyancy-term profile in the dry convective boundary layer driven by the surface buoyancy flux (case FC, Figure 1). Both profiles are linear with the negative buoyancy flux due to entrainment at the top of the respective layer. The buoyancy production of TKE is large within the cloud layer in both CTBLs. This is attributed to the release of latent heat during the cloud formation process. In the DYCOMS case, there is an additional kinetic-energy production mechanism due to the cloud top long-wave radiation cooling, leading to the top-down negatively buoyant thermals. At the top of the mixed layer which is at $x_3 = 500$ m for BOMEX and $x_3 = 850$ m for DYCOMS, $\mathcal{B}_{TKE}$ is negative. In these regions, TKE is destroyed by buoyancy as the warm air from above is entrained into the mixed layers.

The dissipation rate $\mathcal{D}_{TKE}^{re}$ is a major sink of TKE for both CTBLs. It has maxima near the surface and within the cloud layers, where the TKE production by mean-velocity shear and buoyancy, respectively, is most significant.

The turbulent transport terms due to third-order velocity correlations, $\mathcal{T}_{TKE}^{t}$, and the pressure-velocity correlations, $\mathcal{T}_{TKE}^{p}$, redistribute the TKE vertically. They serve as local sources/sinks of TKE, but the total TKE in the boundary layer is not affected (this simply follows from the divergence theorem, see, e.g., *Tennekes and Lumley* [1972, p. 60]).

In the BOMEX case (Figure 4a), the turbulent transport redistributes the TKE from the lower subcloud layer and the lower cumulus cloud layer toward the upper subcloud layer and the upper cloud layer. In the DYCOMS case (Figure 4b), the TKE is transported from the lower subcloud layer and the upper stratocumulus cloud layer toward the upper subcloud layer and lower cloud layer. In both CTBLs, the turbulent transport term $\mathcal{T}_{TKE}^{t}$ is important to maintain the TKE budget in the regions where the buoyancy production of the TKE is small (or the buoyancy flux is negative, i.e., the TKE is spent to work against the gravity).
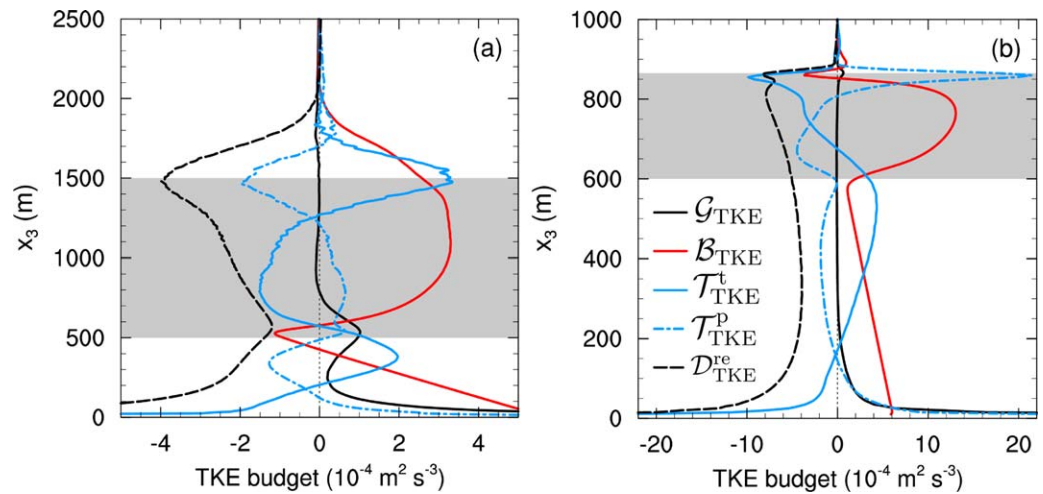
Figure 4. Vertical profiles of terms in the TKE budget for (a) BOMEX and (b) DYCOMS. Notation is given in section 3.1. The dissipation rate $\mathcal{D}^{re}_{TKE}$ is determined with the residual method. The storage term $\mathcal{M}_{TKE}$ is negligibly small and is not plotted. Gray shading and time averaging as in Figure 3.

In the BOMEX case (Figure 4a), the profile of the pressure transport term $\mathcal{T}^{p}_{TKE}$ is somewhat similar in shape to the profile of the (negative of) turbulent transport term $\mathcal{T}^{t}_{TKE}$. This similarity is also seen in DYCOMS (Figure 4b) but only in the subcloud layer. In the stratocumulus-topped boundary layer, $\mathcal{T}^{p}_{TKE}$ reveals a pronounced maximum at the top of the cloud layer, where it is the only source of TKE. In both CTBLs, $\mathcal{T}^{p}_{TKE}$ and $\mathcal{T}^{t}_{TKE}$ tend to compensate each other.

Our results as to the TKE budget are in good agreement with previous LES studies of the cumulus-topped [e.g., *Cuijpers et al.*, 1996; *Brown*, 1999] and the stratocumulus-topped [e.g., *Deardorff*, 1980; *Moeng*, 1986] boundary layers.

3.3.2. Velocity Variances
Vertical profiles of horizontal-velocity variances $UU=\langle \bar{u}_1^{\prime\prime 2}\rangle+\langle \tau_{11}\rangle$ and $VV=\langle \bar{u}_2^{\prime\prime 2}\rangle+\langle \tau_{22}\rangle$ are similar in shape to the TKE profile in both CTBLs (Figure 3). In the BOMEX case (Figure 3a), the vertical-velocity variance $WW=\langle \bar{u}_3^{\prime\prime 2}\rangle+\langle \tau_{33}\rangle$ has a maximum in the middle of the subcloud layer and a second maximum at the top of the cumulus cloud layer. The WW profile in the subcloud layer is very similar in shape to the WW profile in the dry convective boundary layer driven by the surface buoyancy flux (case FC). In the DYCOMS case (Figure 3b), WW has a single maximum very near the stratocumulus layer bottom, indicating that the cloud layer and the subcloud layer are well coupled. Near the top of the stratocumulus layer, convective updrafts impinge on a strongly stable layer (capping inversion) and are deflected sideways, leading to large horizontal-velocity variances at the expense of the vertical-velocity variance.

Vertical profiles of terms in the budgets of the velocity variances are shown in Figure 5. The shear terms $\mathcal{G}_{11}$ and $\mathcal{G}_{22}$ in the UU and VV budgets, respectively, are positive and large in the surface layer in both CTBLs (Figures 5a–5d). Since $\mathcal{G}_{33}=0$, the shear term in the TKE budget is $\mathcal{G}_{TKE}=\frac{1}{2}(\mathcal{G}_{11}+\mathcal{G}_{22})$. That is, the production (destruction) of TKE due to mean-velocity shear occurs through the horizontal velocity components. The buoyancy term $\mathcal{B}_{33}$ is only present in the vertical-velocity variance budget, that is, the production (destruction) of TKE due to buoyancy effects occurs through the vertical velocity component (a discussion of the buoyancy production/destruction of TKE is given in section 3.3.1 and is not repeated here in relation to the WW budget as $\mathcal{B}_{33}$ is just twice $\mathcal{B}_{TKE}$). As the shear and buoyancy production (destruction) of the velocity variances are very different in terms of the magnitude of the respective budget terms and in terms of their vertical structure (the shear production occurs primarily near the underlying surface, whereas the buoyancy production is a maximum in the cloud layer), turbulence turns out to be (strongly) anisotropic.

The anisotropy introduced by shear and buoyancy is counteracted by the pressure-strain correlation $\Pi_{ij}+\mathcal{P}_{ij}$, which is also referred to as the pressure scrambling term. This term is a traceless tensor, see equation (1). Hence, it does not change the TKE but acts to redistribute kinetic energy of turbulence between the components. A detailed discussion of the pressure scrambling term is beyond the scope of the present
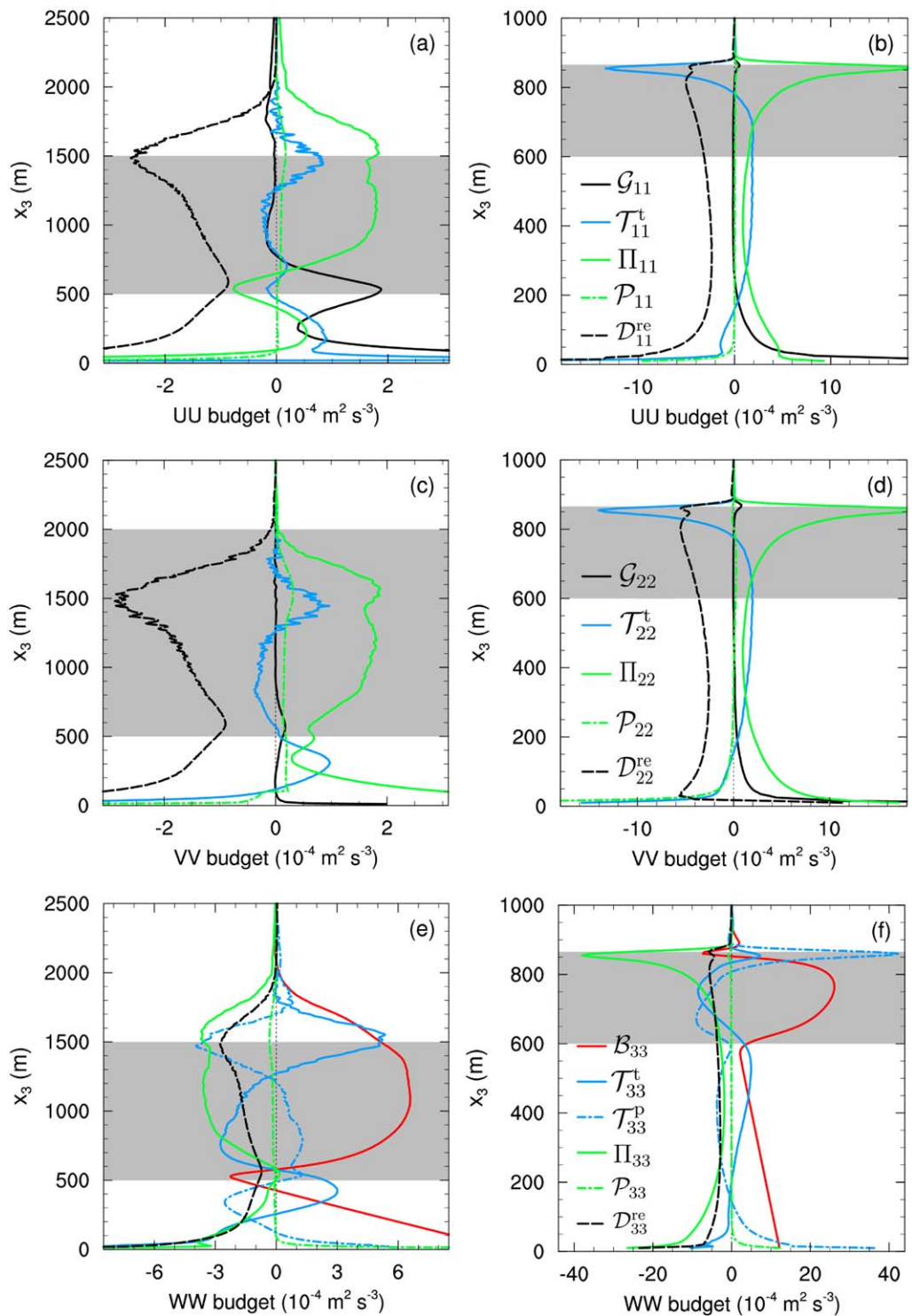
Figure 5. Vertical profiles of terms in the budgets of the horizontal-velocity variances (a and b) UU, (c and d) VV, and (e and f) of the vertical-velocity variance WW. The BOMEX results are shown in the Figures 5a, 5c, and 5e, and the DYCOMS results are shown in the Figures 5b, 5d, and 5f. Legends refer to the plots in each row. Notation is given in section 3.1. The dissipation rates $\mathcal{D}_{11}^{re}$, $\mathcal{D}_{22}^{re}$, and $\mathcal{D}_{33}^{re}$ are determined with the residual method. The Coriolis terms $\mathcal{C}_{11}$, $\mathcal{C}_{22}$, and $\mathcal{C}_{33}$ and the storage terms $\mathcal{M}_{11}$, $\mathcal{M}_{22}$, and $\mathcal{M}_{33}$ are negligibly small and are not plotted. Gray shading and time averaging as in Figure 3.

study; this will be the subject of a subsequent paper. Here we note that the major effect of the pressure scrambling term is to return turbulence to an isotropic state, where the TKE is evenly distributed between its components [e.g., *Pope*, 2000; *Hanjalić and Launder*, 2011]. As seen from Figure 5, $\Pi_{11}+\mathcal{P}_{11}$ and $\Pi_{22}+\mathcal{P}_{22}$ are positive and $\Pi_{33}+\mathcal{P}_{33}$ is negative throughout most of the boundary layer in both CTBLs. This suggests that the horizontal-velocity variances UU and VV grow at the expense of the vertical-velocity variance WW which is produced by buoyancy. In the vicinity of the underlying surface, kinetic energy produced by the mean-velocity shear is redistributed by the pressure scrambling effects from the horizontal components to the vertical component (cf. a discussion in *Cuijpers et al.* [1996]). Figure 5 also shows that the SGS pressure scrambling term $\mathcal{P}_{ij}$ is small over most of the CTBLs except for the surface layer where it should be accounted for to close the budgets to a good order [cf. *Khanna*, 1998; *Mironov*, 2001]. The SGS contributions to the mean-gradient, buoyancy and transport terms are not plotted separately. They are negligibly small over most of the domain (except very close to the surface).

The dissipation rates in the UU, VV, and WW budgets are determined by means of the residual method from the following relations:

$$\mathcal{D}_{11}^{\mathrm{re}}=-\mathcal{G}_{11}-\mathcal{C}_{11}-\mathcal{T}_{11}^{\mathrm{t}}-\Pi_{11}-\mathcal{P}_{11}+\mathcal{M}_{11}, \tag{8}$$

$$\mathcal{D}_{22}^{\mathrm{re}}=-\mathcal{G}_{22}-\mathcal{C}_{22}-\mathcal{T}_{22}^{\mathrm{t}}-\Pi_{22}-\mathcal{P}_{22}+\mathcal{M}_{22}, \tag{9}$$

and

$$\mathcal{D}_{33}^{\mathrm{re}}=-\mathcal{B}_{33}-\mathcal{T}_{33}^{\mathrm{t}}-\mathcal{T}_{33}^{\mathrm{p}}-\Pi_{33}-\mathcal{P}_{33}+\mathcal{M}_{33}. \tag{10}$$

The dissipation rate is the main sink in the horizontal-velocity variance budgets (Figures 5a–5d). In the vertical-velocity variance budget of BOMEX (Figure 5e), the dissipation rate is of the same order of magnitude as the pressure scrambling term Π_{33}, both terms act to reduce WW. This is also the case for DYCOMS (Figure 5f), but the loss of WW in the upper stratocumulus layer is dominated by the pressure scrambling term. This difference in the relative importance of the dissipation and the pressure redistribution between the cumulus-topped and the stratocumulus-topped boundary layers was also observed by *Golaz et al.* [2005]. They argue that the pressure redistribution becomes more important in maintaining the WW budget when a strong capping inversion is present. The inversion is indeed stronger in DYCOMS than in BOMEX.

A comparison of $\mathcal{D}_{11}^{\mathrm{re}}$, $\mathcal{D}_{22}^{\mathrm{re}}$, and $\mathcal{D}_{33}^{\mathrm{re}}$ (Figure 5) and $\mathcal{D}_{\mathrm{TKE}}^{\mathrm{re}}$ (Figure 4) shows that the residual method (along with high resolution of our LES runs) is capable of producing the kinetic energy dissipation rate estimates that are compatible with the assumption of local isotropy at small scales, i.e., $\mathcal{D}_{11}^{\mathrm{re}}\approx\mathcal{D}_{22}^{\mathrm{re}}\approx\mathcal{D}_{33}^{\mathrm{re}}\approx\frac{2}{3}\mathcal{D}_{\mathrm{TKE}}^{\mathrm{re}}$. A positive $\mathcal{D}_{22}^{\mathrm{re}}$ in Figure 5d is an artifact, indicating a limited reliability of LES near the surface.

The turbulent transport terms $\mathcal{T}_{11}^{\mathrm{t}}$ and $\mathcal{T}_{22}^{\mathrm{t}}$ are less important for maintaining the UU and VV budgets, respectively, in the cumulus-topped boundary layer than the dissipation and the pressure redistribution terms (Figures 5a and 5c). In the stratocumulus-topped boundary layer (Figures 5b and 5d), the turbulent transport is as important as the dissipation and the pressure redistribution. It is particularly important at the cloud layer top, where it is a major sink of the horizontal-velocity variances, whereas the pressure redistribution is a major source. The turbulent transport term $\mathcal{T}_{33}^{\mathrm{t}}$ is the leading-order term in the budget of the vertical-velocity variance in both CTBLs (Figures 5e and 5f). A comparison of Figures 5 and 4 suggests that $\mathcal{T}_{33}^{\mathrm{t}}$ makes a major contribution to the turbulent transport term $\mathcal{T}_{\mathrm{TKE}}^{\mathrm{t}}$ in the TKE budget. This result corroborates previous findings based on the LES of cumulus-topped boundary layers [*Cuijpers et al.*, 1996] and on the observations taken in a dry convective boundary layer [*Lenschow et al.*, 1980].

Our results as to the budgets of the velocity variances are generally in good agreement with previous findings of *Moeng* [1986], *Cuijpers et al.* [1996], *de Roode and Bretherton* [2003], and *Golaz et al.* [2005].

3.3.3. Momentum Fluxes

A remark is in order concerning the interpretation of the flux budget terms. As different from the velocity and scalar variances that are nonnegative, fluxes can have either sign. Then, the flux-budget term is a source of the flux in question where it has the same sign as the flux itself (e.g., a negative flux-budget term is a source where the flux is negative), and the budget term is a sink if its sign is opposite to the sign of the flux.

Vertical profiles of momentum fluxes (off-diagonal terms of the Reynolds-stress tensor) WU$=\langle\bar{u}_3''\bar{u}_1''\rangle+\langle\tau_{13}\rangle$ and WV$=\langle\bar{u}_3''\bar{u}_2''\rangle+\langle\tau_{23}\rangle$ are shown in Figure 6. In the BOMEX case (Figure 6a), WU and WV decrease with
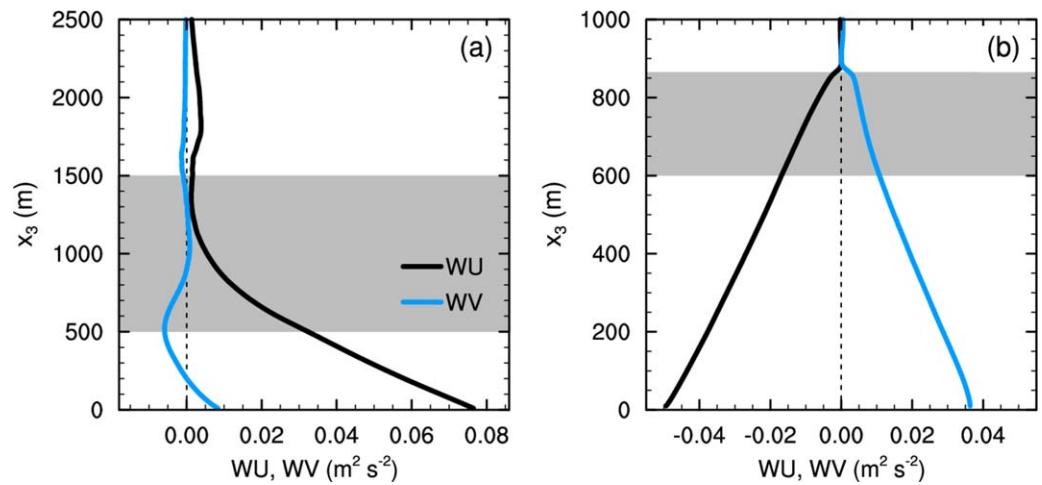
Figure 6. Vertical profiles of momentum fluxes WU$=\langle \bar{u}_3'' \bar{u}_1'' \rangle + \langle \tau_{13} \rangle$ (black lines) and WV$=\langle \bar{u}_3'' \bar{u}_2'' \rangle + \langle \tau_{23} \rangle$ (blue lines) for (a) BOMEX and (b) DYCOMS. Gray shading and time averaging as in Figure 3.

height in the subcloud layer and are nearly zero in the upper part of the cloud layer. WU is much larger than WV in the subcloud layer and in the lower half of the cloud layer. This can be attributed to the fact that the trade winds of BOMEX are dominated by the zonal wind component [see *Siebesma et al.*, 2003]. In the DYCOMS case (Figure 6b), WU and WV change almost linearly with height throughout the subcloud and cloud layers, indicating that the two layers are well coupled. The boundary-layer wind blows from north-westerly directions, resulting in a negative WU and a positive WV.

Vertical profiles of terms in the budgets of WU and WV are shown in Figure 7. The budget terms fluctuate strongly within and above the cumulus layer of BOMEX (Figures 7a and 7c). In order to obtain more smooth budget terms, (much) larger domain size and averaging time are necessary [cf. *Lenschow and Stankov*, 1986]. Note that in the BOMEX case a detailed analysis of the WV budget above $x_3 = 1000$ m is hardly possible (and hardly necessary) because WV itself is small.

In both CTBLs, the shear, $\mathcal{G}_{13}$ and $\mathcal{G}_{23}$, and the buoyancy, $\mathcal{B}_{13}$ and $\mathcal{B}_{23}$, terms are the major momentum-flux production terms in the lower part of the subcloud layer (approximately at $x_3 < 200$ m for BOMEX, and at $x_3 < 400$ m for DYCOMS). These production terms are balanced by the pressure transport, $\mathcal{T}_{13}^p$ and $\mathcal{T}_{23}^p$, and the pressure redistribution, $\Pi_{13} + \mathcal{P}_{13}$ and $\Pi_{23} + \mathcal{P}_{23}$, terms and, to a lesser extent, by the turbulent transport terms, $\mathcal{T}_{13}^t$ and $\mathcal{T}_{23}^t$. In the upper part of the subcloud layer and the lower part of the cloud layer of BOMEX (Figure 7a), the shear term is a major source of WU, whereas the pressure redistribution and the buoyancy terms are major sinks. In the upper part of the cumulus layer and in the inversion aloft, $\mathcal{G}_{13}$ is a major sink and $\mathcal{B}_{13}$ is a major source of WU. In the DYCOMS case (Figures 7b and 7d), the budgets of WU and WV near the surface are dominated by the shear and buoyancy terms (sources) and the pressure transport and pressure redistribution terms (sinks). Near the top of the stratocumulus layer, where the budget terms are maximal, the buoyancy destruction of WU and WV is balanced (in order of importance) by the pressure transport, pressure redistribution and shear effects.

The Coriolis terms $\mathcal{C}_{13}$ and $\mathcal{C}_{23}$ (not shown in Figure 7) proved to be negligibly small. The residuals of the WU and WV budgets,

$$\mathcal{R}_{13} = \mathcal{G}_{13} + \mathcal{B}_{13} + \mathcal{C}_{13} + \mathcal{T}_{13}^t + \mathcal{T}_{13}^p + \Pi_{13} + \mathcal{P}_{13} - \mathcal{M}_{13}, \tag{11}$$

and

$$\mathcal{R}_{23} = \mathcal{G}_{23} + \mathcal{B}_{23} + \mathcal{C}_{23} + \mathcal{T}_{23}^t + \mathcal{T}_{23}^p + \Pi_{23} + \mathcal{P}_{23} - \mathcal{M}_{23}, \tag{12}$$

respectively, are small throughout both CTBLs except in the near vicinity of the surface. However, $\mathcal{R}_{13}$ and $\mathcal{R}_{23}$ near the surface are still smaller than the leading-order budget terms. The SGS pressure terms $\mathcal{P}_{13}$ and $\mathcal{P}_{23}$ are not negligible in the surface layer.
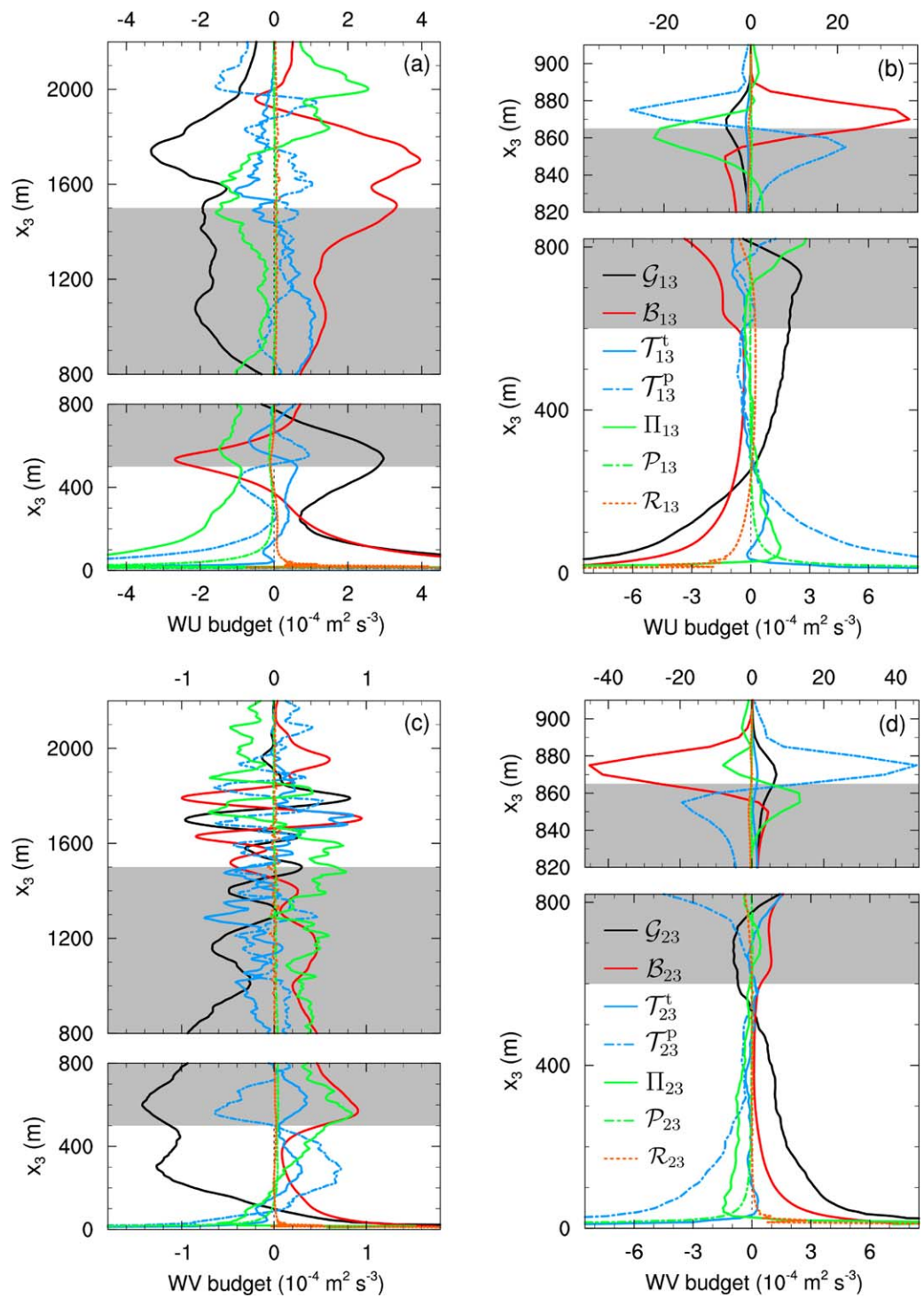
Figure 7. Vertical profiles of terms in the budgets of the zonal momentum flux (a and b) WU and of the meridional momentum flux (c and d) WV. The BOMEX results are shown in the Figures 7a and 7c, and the DYCOMS results are shown in the 7b and 7d. Legends refer to the plots in each row. Notation is given in section 3.1. $\mathcal{R}_{13}$ and $\mathcal{R}_{23}$ denote the budget residuals. The Coriolis terms $\mathcal{C}_{13}$ and $\mathcal{C}_{23}$ and the storage terms $\mathcal{M}_{13}$ and $\mathcal{M}_{23}$ are negligibly small and are not plotted. Ordinates are stretched near the cloud layer top. Different abscissa scales are used for lower and upper parts of the boundary layer in Figures 7b and 7d. Gray shading and time averaging as in Figure 3.

It should be noted that the momentum-flux budgets have been rarely analyzed so far. The WU and WV budget analysis based on observations in stratocumulus-topped boundary layers by *Brost et al.* [1982] reveals, in agreement with the present results, the dominant role of the shear terms $\mathcal{G}_{13}$ and $\mathcal{G}_{23}$ and the
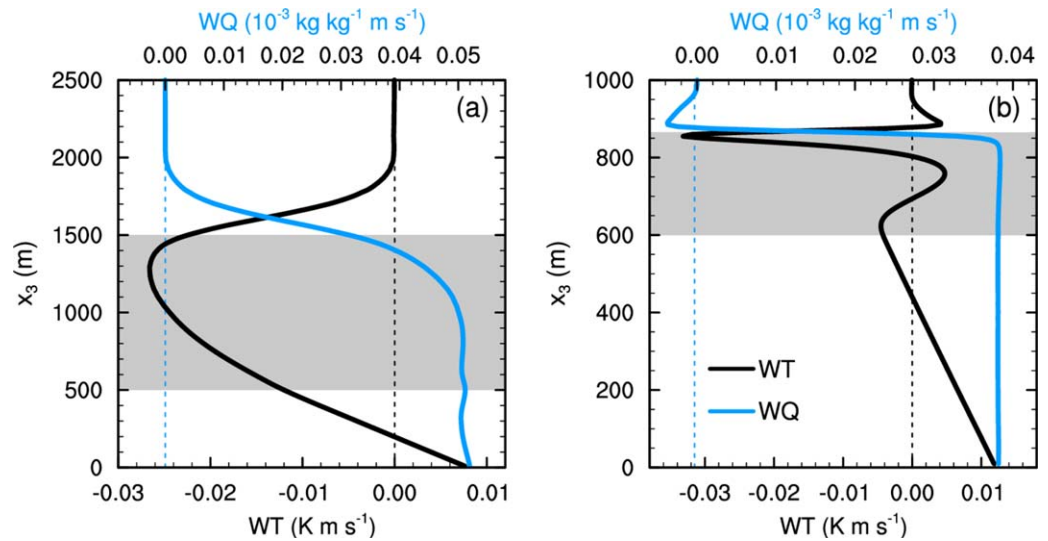
Figure 8. Vertical profiles of the liquid water potential temperature flux WT$=\langle \bar{u}_3'' \bar{\theta}_l'' \rangle + \langle \tau_{\theta 3} \rangle$ (black lines) and of the total water specific humidity flux WQ$=\langle \bar{u}_3'' \bar{q}_t'' \rangle + \langle \tau_{q3} \rangle$ (blue lines) for (a) BOMEX and (b) DYCOMS. Thin dashed vertical lines indicate zero fluxes: WT=0 (black) and WQ=0 (blue). Gray shading and time averaging as in Figure 3.

importance of the buoyancy destruction of the momentum flux near the top of the boundary layer. It also suggests that the turbulent transport is of minor importance in maintaining the momentum-flux budget. Simulations with a third-order turbulence closure model by *Therry and Lacarrere* [1983] show that the shear, buoyancy, transport and pressure redistribution terms are maximal near the boundary-layer top. Results from *Wyngaard*, [2010, p. 250] illustrate that the effects of shear, pressure redistribution and pressure transport dominate the momentum-flux budgets. These results are in agreement with our findings.

3.3.4. Scalar Fluxes

Vertical fluxes of the liquid water potential temperature, WT$=\langle \bar{u}_3'' \bar{\theta}_l'' \rangle + \langle \tau_{\theta 3} \rangle$, and of the total water specific humidity, WQ$=\langle \bar{u}_3'' \bar{q}_t'' \rangle + \langle \tau_{q3} \rangle$, are shown in Figure 8. In both CTBLs, WT in the subcloud layer (where there is no liquid water so that WT reduces to the flux of potential temperature, $\langle \bar{u}_3'' \bar{\theta}'' \rangle + \langle \overline{u_3' \theta'} \rangle$) is to a good approximation linear, indicating that the subcloud layer is well mixed. The WT profile in the subcloud layer, with a positive flux at the surface and a negative flux at the subcloud layer top, resembles the WT profile in the dry convective boundary layer driven by the surface buoyancy flux (case FC). In both BOMEX and DYCOMS, WT is a minimum just below the cloud top and increases to zero aloft. The total water specific humidity flux WQ is positive and nearly height-constant over the subcloud layer and over most of the cloud layer in both cases. This indicates that most of the moisture from the ocean surface is transported toward the upper part of the cloud layer. Then, WQ rapidly decreases and approaches zero above the cloud top. The profiles of WT and WQ reveal an overshooting just above the stratocumulus layer (Figure 8b). This feature is most likely purely numerical and can be attributed to the use of a nonmonotonic advection scheme.

Vertical profiles of terms in the budgets of WT and WQ are shown in Figure 9. The budget terms have their extrema near the surface and in the interfacial layer. These are the regions where large vertical gradients of $\bar{\theta}_l$ and $\bar{q}_t$ occur. Notice that the budget terms in the inversion layer are one (BOMEX) and three (DYCOMS) orders of magnitude larger than in the subcloud layer.

The mean gradient term $\mathcal{G}_{\theta 3}^{\theta}$ in the WT budget (Figures 9a and 9b) and the liquid water potential temperature gradient $\partial \langle \bar{\theta}_l \rangle / \partial x_3$ have opposite signs (see equation (3)). $\mathcal{G}_{\theta 3}^{\theta}$ generates positive (upward) liquid water potential temperature flux near the surface and negative (downward) flux in the cumulus and stratocumulus layers. The buoyancy term $\mathcal{B}_{\theta 3}$ is positive throughout most of the CTBLs. It (mostly) generates positive (upward) WT. Due to the effect of buoyancy, the downward WT becomes less negative at the top of the
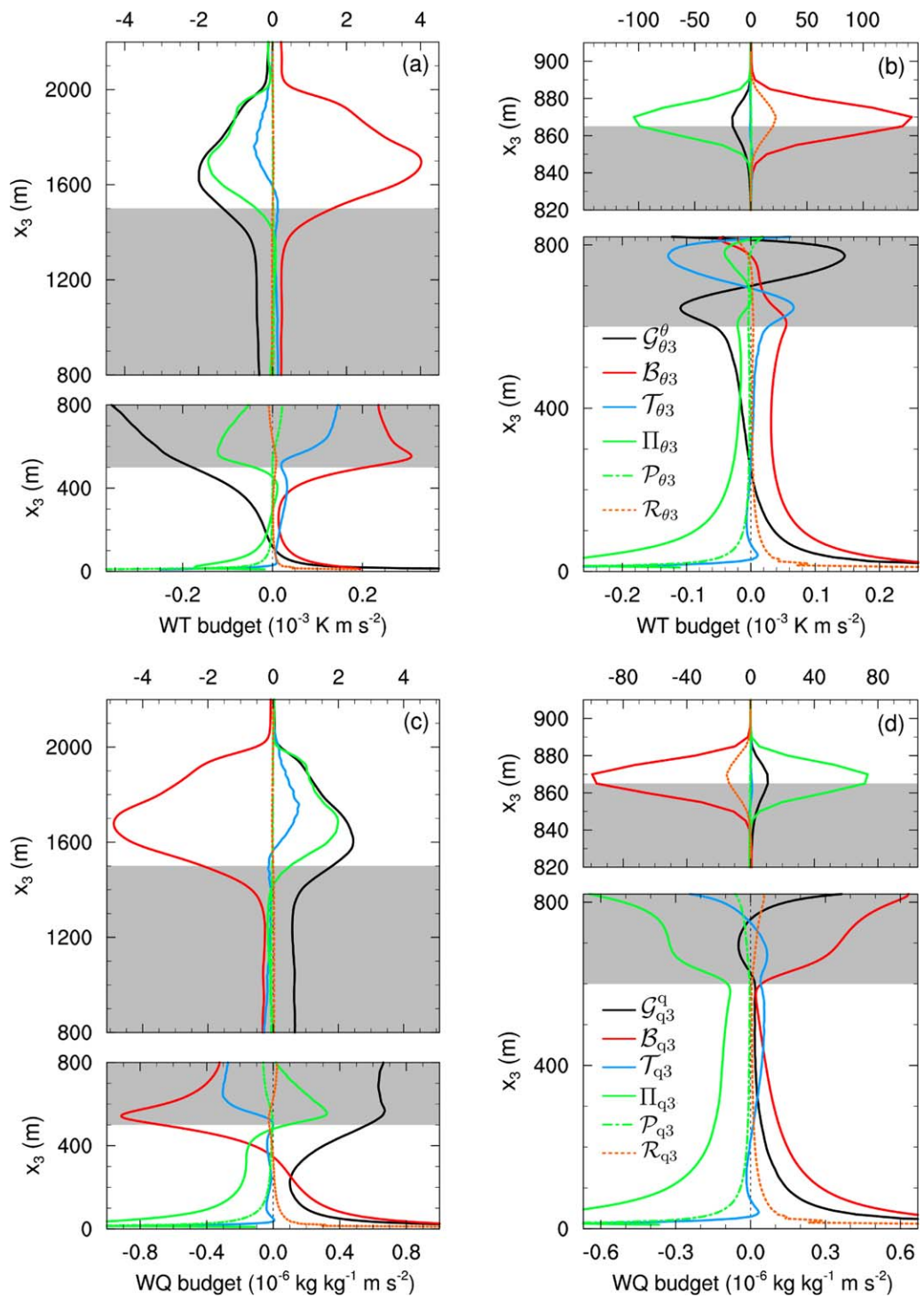
Figure 9. Vertical profiles of terms in the budgets of the liquid water potential temperature flux (a and b) WT, and of the total water specific humidity flux (c and d) WQ. The BOMEX results are shown in the Figures 9a and 9c, and the DYCOMS results are shown in the Figures 9b and 9d. Legends refer to the plots in each row. Notation is given in section 3.1. $\mathcal{R}_{\theta 3}$ and $\mathcal{R}_{q 3}$ denote the budget residuals. The storage terms $\mathcal{M}_{\theta 3}$ and $\mathcal{M}_{q 3}$ are negligible and are not plotted. Ordinates are stretched near the cloud layer top. Different abscissa scales are used for lower and upper parts of the boundary layer. Gray shading and time averaging as in Figure 3.

cloud layer and in the inversion. One more leading-order term is the pressure gradient-liquid water potential temperature covariance $\Pi_{\theta 3} + \mathcal{P}_{\theta 3}$. This "pressure scrambling" term is vitally important in maintaining the WT budget in both CTBLs. The turbulent transport term $\mathcal{T}_{\theta 3}$ is of secondary importance.

Similarly to the WT budget, the budget of WQ (Figures 9c and 9d) is dominated by the mean-gradient, buoyancy, and pressure scrambling (pressure gradient-total water specific humidity covariance) terms. Since $\langle \bar{q}_t \rangle$ is a monotonically decreasing function of height, the mean-gradient term $\mathcal{G}_{q3}^q$ is positive throughout both CTBLs. The only exception is the lower part of the stratocumulus layer, where $\partial \langle \bar{q}_t \rangle / \partial x_3$ is slightly positive. Thus, $\mathcal{G}_{q3}^q$ generates positive (upward) WQ throughout (most of) the CTBLs. The buoyancy term $\mathcal{B}_{q3}$ changes sign. It generates positive WQ in the subcloud layer of BOMEX and in the subcloud layer and the lower part of the stratocumulus layer of DYCOMS. Within the cumulus layer, in the upper part of the strato-cumulus layer and above the cloud layers in both CTBLs, $\mathcal{B}_{q3}$ becomes a sink of WQ. Apart from the mean-gradient and the buoyancy terms, the pressure scrambling term $\Pi_{q3} + \mathcal{P}_{q3}$ is vitally important in maintaining the WQ budget in both cases. The turbulent transport term $\mathcal{T}_{q3}$ is of secondary importance. Note that the profile of the buoyancy term somewhat resembles the profile of the (negative of) pressure scrambling term, particularly in the DYCOMS case [cf. *Cuijpers et al.*, 1996; *Moeng*, 1986].

The budget residuals

$$\mathcal{R}_{\theta 3} = \mathcal{G}_{\theta 3}^\theta + \mathcal{B}_{\theta 3} + \mathcal{T}_{\theta 3} + \Pi_{\theta 3} + \mathcal{P}_{\theta 3} - \mathcal{M}_{\theta 3}, \tag{13}$$

and

$$\mathcal{R}_{q 3} = \mathcal{G}_{q 3}^q + \mathcal{B}_{q 3} + \mathcal{T}_{q 3} + \Pi_{q 3} + \mathcal{P}_{q 3} - \mathcal{M}_{q 3}, \tag{14}$$

are small over most of the boundary layer in both cases, except in the vicinity of the surface. Notice that in DYCOMS the residual near the cloud top is nonnegligible. Results from a grid resolution sensitivity study (not shown) suggest that the mean-gradient terms increase and the budget residuals decrease as the grid spacing is reduced. At a grid spacing of 5 m used in the present study, PALM still has some problems to handle very large scalar gradients in the interfacial layer. The SGS pressure terms $\mathcal{P}_{\theta 3}$ and $\mathcal{P}_{q 3}$ appear to be nonnegligible near the surface and should be accounted for to close the scalar-flux budgets to a good order. The SGS contributions to the mean-gradient, buoyancy, and turbulent transport terms (not shown) reveal a similar behavior as the SGS pressure terms. They are, however, smaller than the SGS pressure terms over most of the domain.

3.3.5. Scalar Variances and Covariance

Vertical profiles of 1/2 of the scalar variances, $\mathrm{TT} = \frac{1}{2} \left(\langle \overline{\theta_l^{''2}} \rangle + \langle \tau_{\theta\theta} \rangle \right)$ and $\mathrm{QQ} = \frac{1}{2} \left(\langle \overline{q_t^{''2}} \rangle + \langle \tau_{qq} \rangle \right)$, and of the scalar covariance, $\mathrm{QT} = \langle \overline{q_t^{''} \theta_l^{''}} \rangle + \langle \tau_{\theta q} \rangle$, where $\tau_{\theta\theta} = \overline{\theta_l^{'2}}$ and $\tau_{qq} = \overline{q_t^{'2}}$ are the SGS variances of the liquid water potential temperature and the total water specific humidity, respectively, are shown in Figure 10.

In the DYCOMS case (Figure 10b), the scalar variances and covariance have their extrema near the surface and at the cloud layer top. At the top of the stratocumulus layer, TT, QQ, and QT are several orders of magnitude larger than below. In the BOMEX case (Figure 10a), QQ has a maximum near the surface and more pronounced maxima at the bottom of the cloud layer and just above the top of the cloud layer, whereas TT has a single pronounced maximum just above the cloud top. The scalar covariance QT also has a single pronounced extremum (minimum) just above the cloud top. The most pronounced extrema of variances and covariance are encountered in the regions, where vertical gradients of $\langle \bar{\theta}_l \rangle$ and $\langle \bar{q}_t \rangle$ are largest (in magnitude).

The scalar covariance QT is positive near the surface in both BOMEX and DYCOMS. The rising air parcels near the surface are warmer ($\bar{\theta}_l^{''} > 0$) and more humid ($\bar{q}_t^{''} > 0$) than their surrounding, leading to a positive QT. The covariance becomes negative at a certain height (ca. $x_3 = 100$ m for BOMEX, and ca. $x_3 = 300$ m for DYCOMS). Inside the cumulus layer, the cloudy air is cooler ($\bar{\theta}_l^{''} < 0$) and more humid ($\bar{q}_t^{''} > 0$) than the horizontal mean and the environment air is warmer ($\bar{\theta}_l^{''} > 0$) and dryer ($\bar{q}_t^{''} < 0$) than the mean, resulting in a negative QT [*Cuijpers et al.*, 1996]. In the stratocumulus layer, the properties of saturated and unsaturated air with respect to the horizontal mean are the same as in the cumulus layer (cool and humid versus warm and dry), but the fractional area coverage of the saturated (cloudy) air is much larger in the stratocumulus case.

Vertical profiles of terms in the budgets of scalar variances TT and QQ are shown in Figure 11. The dissipation terms $\mathcal{D}_{\theta\theta}$ and $\mathcal{D}_{qq}$ are negative definite and are the sink terms throughout the CTBLs. The mean-gradient terms $\mathcal{G}_{\theta\theta}$ and $\mathcal{G}_{qq}$ are large source terms near the surface in both cases, near the upper part of the stratocumulus layer, and within and just above the cumulus layer. In the middle of the subcloud layer, the mean-gradient terms in both TT budgets and in the DYCOMS QQ budget are small or even negative. A
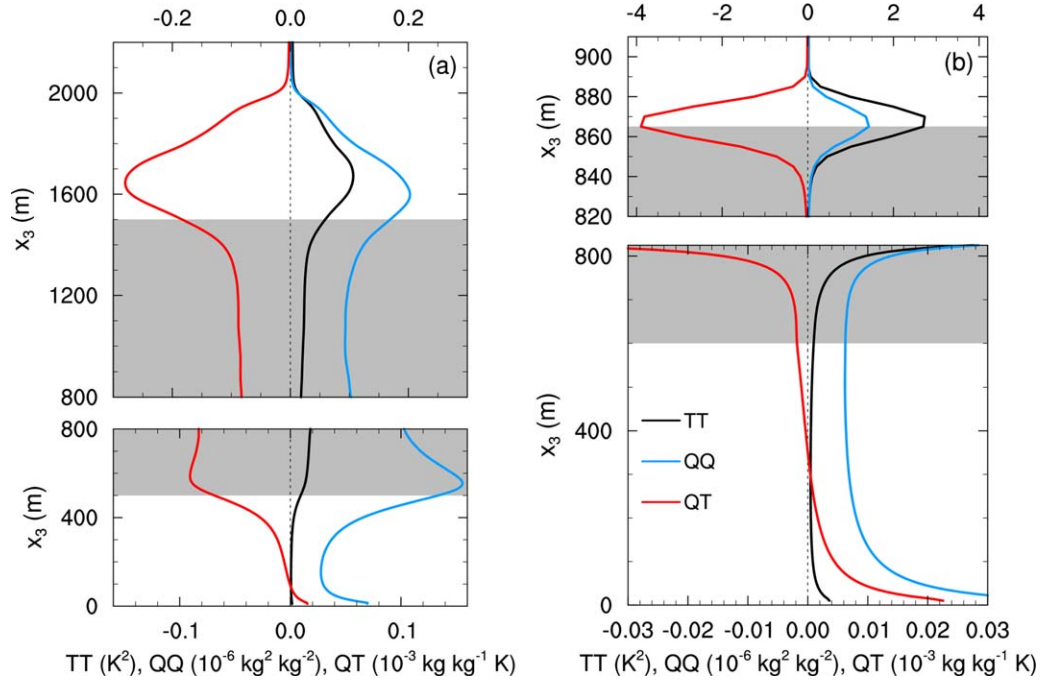
Figure 10. Vertical profiles of 1/2 of the liquid water potential temperature variance, $TT = \frac{1}{2}\left(\langle\bar{\theta}_l''^2\rangle + \langle\tau_{\theta\theta}\rangle\right)$ (black lines), of 1/2 of the total water specific humidity variance, $QQ = \frac{1}{2}\left(\langle\bar{q}_t''^2\rangle + \langle\tau_{qq}\rangle\right)$ (blue lines), and of the covariance of these scalars, $QT = \langle\bar{q}_t''\bar{\theta}_l''\rangle + \langle\tau_{\theta q}\rangle$ (red lines), for (a) BOMEX and (b) DYCOMS. Ordinates are stretched near the cloud layer top. Different abscissa scales are used for lower and upper parts of the boundary layer. Gray shading and time averaging as in Figure 3.

negative mean-gradient term indicates a counter-gradient scalar transport (the scalar flux and the scalar gradient have the same sign). Where $\mathcal{G}_{\theta\theta}$ or $\mathcal{G}_{qq}$ becomes a sink, the scalar-variance budget is maintained by the turbulent transport, terms $\mathcal{T}_{\theta\theta}$ and $\mathcal{T}_{qq}$ (see equation (4)). The turbulent transport terms are also important within and just above the cloud layers, where they are of the same order of magnitude as the mean-gradient (source) and the dissipation (sink) terms. Thus, the turbulent transport is crucial in maintaining the scalar-variance budgets throughout both CTBLs.

The scalar-variance budget residuals

$$\mathcal{R}_{\theta\theta} = \mathcal{G}_{\theta\theta} + \mathcal{T}_{\theta\theta} + \mathcal{D}_{\theta\theta} - \mathcal{M}_{\theta\theta}, \tag{15}$$

and

$$\mathcal{R}_{qq} = \mathcal{G}_{qq} + \mathcal{T}_{qq} + \mathcal{D}_{qq} - \mathcal{M}_{qq}, \tag{16}$$

are small in the BOMEX case (Figures 11a and 11c), except in the vicinity of the surface where LES results are known to be less reliable. In the DYCOMS case (Figures 11b and 11d), $\mathcal{R}_{\theta\theta}$ and $\mathcal{R}_{qq}$ near the top of the stratocumulus layer are of the same order of magnitude as the mean-gradient terms. The grid spacing used in the present study is still too large to resolve very large scalar gradients at the stratocumulus layer top (see a discussion of WT and WQ budgets in section 3.3.4). Furthermore, the numerical diffusion discussed in section 3.2 adversely effects the scalar-variance estimates [see also *Maronga et al.*, 2013]. Excessive numerical diffusion results in too smooth temperature and humidity fields, which in turn leads to an underestimation of the scalar-variance dissipation rates $\mathcal{D}_{\theta\theta}$ and $\mathcal{D}_{qq}$ particularly near the stratocumulus layer top.

Our findings as to the TT and QQ budgets are in good agreement with previous results of *Deardorff* [1974b], *de Roode and Bretherton* [2003], and *Neggers* [2009].

Vertical profiles of terms in the QT budget are shown in Figure 12. The two mean-gradient terms, $\mathcal{G}_{q\theta}^{q}$ and $\mathcal{G}_{q\theta}^{\theta}$ (see equation (5)), are of the same order of magnitude. They generate positive QT near the surface and negative QT within the cloud layers. Most of the QT production is balanced by the molecular destruction (dissipation) $\mathcal{D}_{q\theta}$. Note that, as different from the scalar-variance dissipation that is negative definite, $\mathcal{D}_{q\theta}$
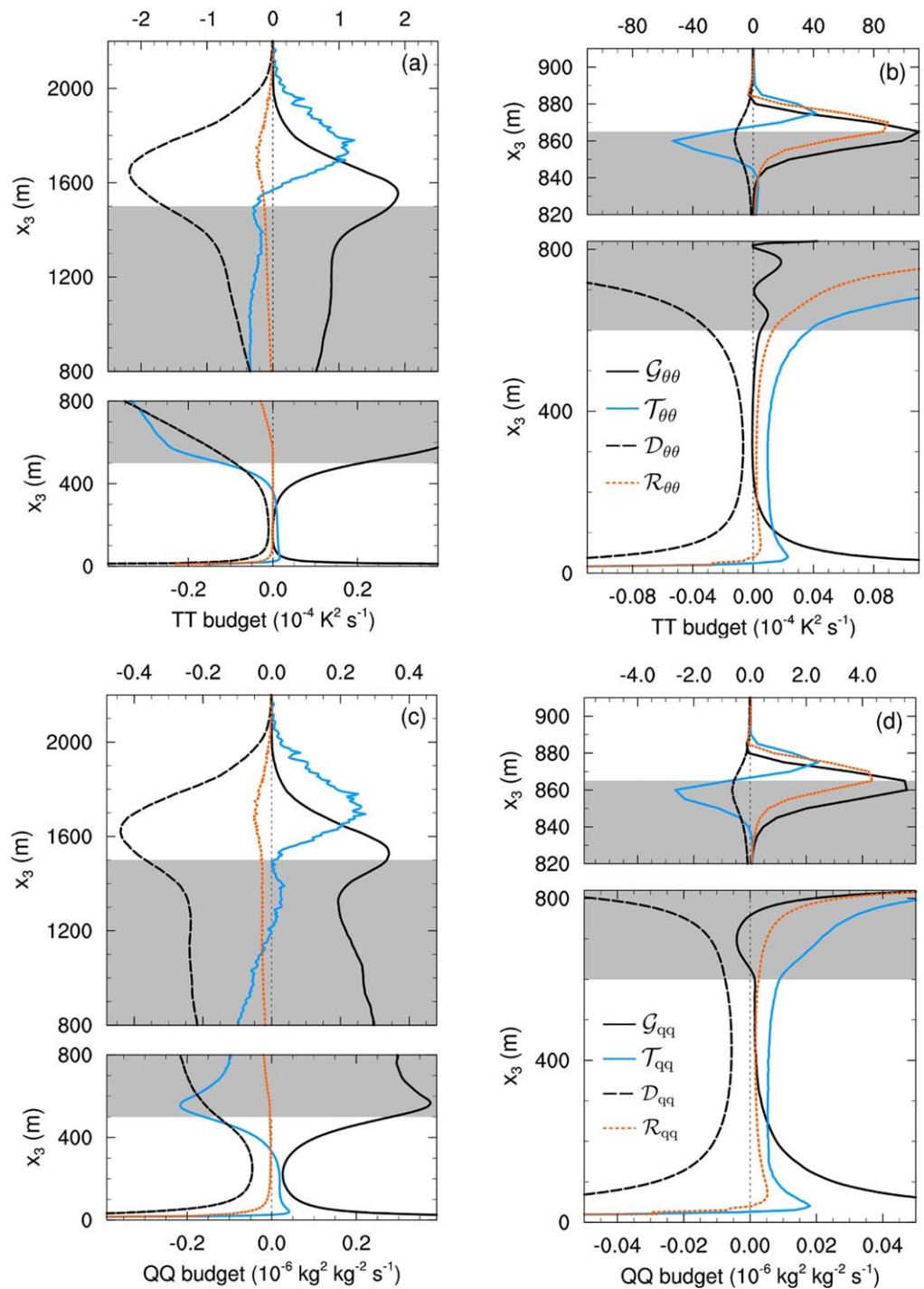
Figure 11. Vertical profiles of terms in the budgets of scalar variances (a and b) TT and (c and d) QQ. The BOMEX results are shown in the Figures 11a and 11c, and the DYCOMS results are shown in the Figures 11b and 11d. Legends refer to the plots in each row. Notation is given in section 3.1. $\mathcal{R}_{\theta\theta}$ and $\mathcal{R}_{qq}$ denote the budget residuals. The storage terms $\mathcal{M}_{\theta\theta}$ and $\mathcal{M}_{qq}$ are negligible and are not plotted. Ordinates are stretched near the cloud layer top. Different abscissa scales are used for lower and upper parts of the boundary layer. Gray shading and time averaging as in Figure 3.

can have either sign [see *Andreas*, 1987]. The turbulent transport term $\mathcal{T}_{q\theta}^{q}$ is somewhat smaller in magnitude than the mean-gradient and the dissipation terms. However, it also plays an important part in maintaining the QT budget, except in the surface layer where the gradient production and the dissipation dominate.
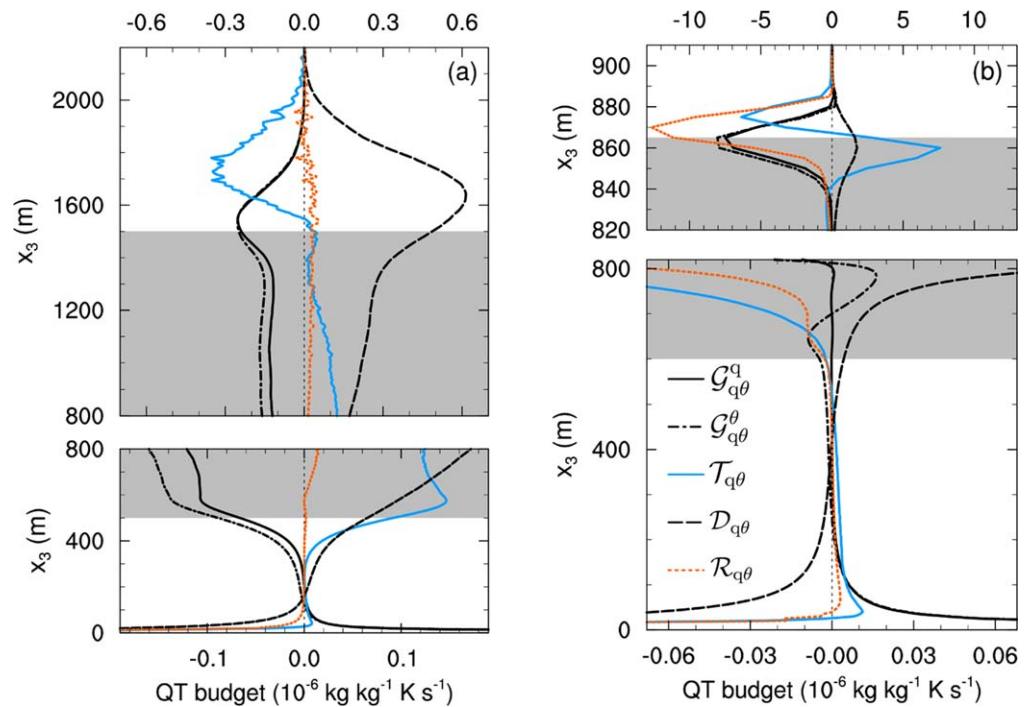
Figure 12. Vertical profiles of terms in the budget of scalar covariance QT for (a) BOMEX and (b) DYCOMS. Notation is given in section 3.1. $\mathcal{R}_{q\theta}$ denotes the budget residual. The storage term $\mathcal{M}_{q\theta}$ is negligible and is not plotted. Ordinates are stretched near the cloud layer top. Different abscissa scales are used for lower and upper parts of the boundary layer. Gray shading and time averaging as in Figure 3.

The QT budget residual

$$\mathcal{R}_{q\theta} = \mathcal{G}^{q}_{q\theta} + \mathcal{G}^{\theta}_{q\theta} + \mathcal{T}_{q\theta} + \mathcal{D}_{q\theta} - \mathcal{M}_{q\theta}, \tag{17}$$

is small over most of the CTBLs, except in the vicinity of the surface in both cases and near the stratocumulus layer top (cf. the residuals of the scalar-variance budgets).

It should be noted that the budget of the scalar covariance QT in CTBLs has not been analyzed so far. Hence, a straightforward comparison of our findings with previous results is not possible. The work of *Wyngaard et al.* [1978] may be mentioned, however. These authors used data from measurements to develop parameterizations of the various terms in the potential temperature-specific humidity covariance budget in the cloud-free convective boundary layer. Some of their findings, e.g., those concerned with the relative importance of the budget terms in the surface layer, are in agreement with the results of the present study.

4. Conclusions

High-resolution large-eddy simulations are used to perform a detailed analysis of the second-order moment budgets in cumulus-topped (BOMEX) and stratocumulus-topped (DYCOMS-II, RF01) boundary-layer flows. Using LES data, terms in the budgets of the Reynolds stress (including its trace, i.e., the TKE), of the vertical fluxes of the liquid water potential temperature and the total water specific humidity, and of the variances and covariance of these two quasi-conservative scalars are estimated. To the best of the authors' knowledge, a comprehensive analysis of these second-moment budgets in cloud topped boundary layers has not been performed so far. Approximations to the ensemble-mean second-moment budgets are computed by averaging the LES data over horizontal planes and over several hundred time steps. Importantly, the LES-based second-moment budgets are computed with due regard for the subgrid scale contributions to the various budget terms [see also *Mironov et al.*, 2000; *Mironov*, 2001; *Mironov and Sullivan*, 2010]. The inclusion of the SGS contributions along with high spatial resolution (grid spacing of 5 m is used) makes it possible to keep the second-moment budget residuals small.

In order to validate the LES results obtained with the large-eddy model PALM, a dry shear-free convective boundary layer driven by the surface buoyancy flux is simulated and the budgets of TKE, of the potential-

temperature variance, and of the vertical potential-temperature flux are computed. Results are compared with the respective budgets obtained by *Mironov et al.* [2000] (their case FC) using a pseudospectral large-eddy model. All budget terms prove to be accurately estimated by PALM except the TKE dissipation rate that is strongly underestimated. This is attributed to the effect of numerical diffusion. The fifth-order advection scheme used by PALM is rather diffusive, leading to smoothed velocity and scalar fields and a reduced energy at scales close to the cutoff wave number, and hence to a reduced transfer of kinetic energy from the resolved scale part of the energy spectrum to the subgrid scale part of the spectrum where the TKE eventually dissipates. Then, underestimation of the scale-interaction term immediately leads to underestimation of the TKE dissipation rate. This behavior was also observed in the Dutch Atmospheric Large-Eddy Simulation model (D. Pino, personal communication, 2011). The use of less diffusive second-order advection scheme yields an improved estimate of the dissipation rate. Having evaluated several methods to estimate the TKE dissipation rate (see section 3.2), we determine it by means of the "residual method," i.e., as a sum of all TKE budget terms except for the dissipation. This method is used in the present study and can also be recommended for LES codes that utilize highly diffusive advection schemes. Note, however, that using the "residual method" all uncertainties associated with the TKE budget are lumped on the dissipation.

Consideration of the TKE budget shows that the buoyancy flux is the major source and the dissipation rate is the major sink of TKE over both CTBLs. The mean-shear production is of major importance only near the surface. The third-order transport and the pressure-transport terms are essential for maintaining the TKE budget, particularly near the cloud top.

The pressure scrambling terms (pressure-strain correlation) play a central role in maintaining the velocity variance budgets. Those terms do not affect the TKE but act to redistribute the energy between the components, driving turbulence to the isotropic state. In the CTBLs considered in the present study, the pressure redistribution terms are responsible for the growth of horizontal-velocity variances at the expense of the vertical-velocity variance. The latter is produced by buoyancy over most of both CTBLs, except in the surface layer where the kinetic energy production due to mean-velocity shear dominates.

The budgets of the momentum-flux components (off-diagonal terms of the Reynolds-stress tensor) are maintained by the mean-velocity shear, buoyancy, pressure scrambling, and pressure transport terms. The third-order turbulent transport appears to be of secondary importance.

The budgets of fluxes of scalar quantities (liquid water potential temperature and total water specific humidity) are dominated by the mean-gradient, buoyancy and pressure-scrambling (pressure gradient-scalar covariance) terms. The third-order turbulent transport appears to be of minor importance for maintaining the scalar-flux budgets.

Along with the mean-scalar-gradient and the dissipation terms, the third-order turbulent transport terms play a key role in maintaining the budgets of variances of the liquid water potential temperature and the total water specific humidity. The same holds true for the budget of covariance of these two quasi-conservative scalars.

The SGS contributions $\mathcal{P}_{ij}$ and $\mathcal{P}_{si}$ to the pressure scrambling terms in the Reynolds-stress and scalar-flux budgets decrease with increasing resolution but remain non-negligible, particularly near the surface. These SGS pressure terms should be accounted for, even at high spatial resolution, to close the LES-based second-moment budgets to a good order.

Results from our analysis of the second-moment budgets have important implications for modeling CTBLs within the second-order closure framework. In particular, the accuracy of description of the CTBL mean and turbulence structure strongly depends on the fidelity of parameterizations of the third-order transport terms in the budgets of scalar variances and covariance and of the pressure scrambling terms in the Reynolds-stress and scalar-flux budgets. A comprehensive analysis of the pressure scrambling terms will be a subject for future work.

Appendix A: Estimation of Ensemble-Mean Second-Moment Budgets Using LES

In what follows, we demonstrate how approximations to the ensemble-mean budgets of the second-order moments are obtained on the basis of numerical data generated by a large-eddy model. As an illustration we examine the budget equation for the scalar variance, equation (4). Budget equations for the other second-order moments are obtained in a similar fashion.

The budget equation for the resolved-scale scalar variance $\langle \bar{s}''^2 \rangle$ is derived in a usual way [cf. *Stull*, 1988, chap. 4.3.2; *Tennekes and Lumley*, 1972, chap. 3], using the transport equation for the filtered scalar quantity $\bar{s}$ (which is either the liquid water potential temperature $\bar{\theta}_l$ or the total water specific humidity $\bar{q}_t$). The equation for $\bar{s}$ reads

$$\frac{\partial \bar{s}}{\partial t} = -\frac{\partial(\bar{u}_i \bar{s})}{\partial x_i} - \frac{\partial \tau_{si}}{\partial x_i} + \bar{Q}_s. \tag{A1}$$

Here, Q_s denotes the source of scalar s, and $\tau_{si} = \overline{u_i' s'}$ is the SGS scalar flux which is computed by the SGS model. Note that we use primes to denote subgrid-scale (more exactly, subfilter scale) fluctuations. Alternatively, the *Lilly* [1967] notation with no primes could be utilized to stress the fact that the filter operator used to derive the LES equations may not satisfy the Reynolds averaging assumptions. Subtracting from equation (A1) its horizontal mean, multiplying the resulting equation by $\bar{s}''$, and averaging the result gives the following equation for the resolved-scale scalar variance:

$$\frac{1}{2}\left(\frac{\partial}{\partial t} + \langle \bar{u}_i \rangle \frac{\partial}{\partial x_i}\right)\langle \bar{s}''^2 \rangle = -\langle \bar{u}_i'' \bar{s}'' \rangle \frac{\partial \langle \bar{s} \rangle}{\partial x_i} - \frac{1}{2}\frac{\partial}{\partial x_i}\langle \bar{u}_i'' \bar{s}''^2 \rangle - \left\langle \bar{s}'' \frac{\partial \tau_{si}''}{\partial x_i} \right\rangle + \langle \bar{s}'' \bar{Q}_s'' \rangle. \tag{A2}$$

The first two terms on the r.h.s. of equation (A2) represent the effects of the mean-gradient production-destruction and of the third-order turbulent transport, respectively, and the last term on the r.h.s. is the correlation of the resolved-scale scalar with the resolved-scale scalar source term. The third term on the r.h.s. is discussed below.

Apart from the resolved-scale variance, the SGS scalar variance $\zeta = \overline{s'^2}$ should be taken into account to close the budget of total variance (resolved plus subgrid) to a good order. Transport equations for various SGS second-order moments are discussed in some detail in *Deardorff* [1973]. Averaging the transport equation for ζ, we obtain

$$\frac{1}{2}\left(\frac{\partial}{\partial t} + \langle \bar{u}_i \rangle \frac{\partial}{\partial x_i}\right)\langle \zeta \rangle = -\left\langle \tau_{si}\frac{\partial \bar{s}}{\partial x_i} \right\rangle - \frac{1}{2}\frac{\partial}{\partial x_i}\left[\langle \bar{u}_i'' \zeta'' \rangle + \langle \overline{u_i' s'^2} \rangle\right] - \langle \epsilon_s \rangle + \langle \overline{s' Q_s'} \rangle. \tag{A3}$$

Here, $\overline{u_i' s'^2}$ is the SGS third-order flux of ζ, and ϵ_s is the dissipation rate of scalar variance. The last term on the r.h.s. of equation (A3) represents the effect of the fluctuating scalar source term on the SGS scalar variance.

Using the relation $\langle ()'' \rangle = 0$ that simply follows from the definition of horizontal averaging, the first term on the r.h.s. of equation (A3) is manipulated to give

$$-\left\langle \tau_{si}\frac{\partial \bar{s}}{\partial x_i} \right\rangle = -\langle \tau_{si} \rangle \frac{\partial \langle \bar{s} \rangle}{\partial x_i} - \frac{\partial}{\partial x_i}\langle \bar{s}'' \tau_{si}'' \rangle + \left\langle \bar{s}'' \frac{\partial \tau_{si}''}{\partial x_i} \right\rangle. \tag{A4}$$

Substituting (A4) into (A3), we obtain

$$\frac{1}{2}\left(\frac{\partial}{\partial t} + \langle \bar{u}_i \rangle \frac{\partial}{\partial x_i}\right)\langle \zeta \rangle = -\langle \tau_{si} \rangle \frac{\partial \langle \bar{s} \rangle}{\partial x_i} - \frac{1}{2}\frac{\partial}{\partial x_i}\left[\langle \bar{u}_i'' \zeta'' \rangle + 2\langle \bar{s}'' \tau_{si}'' \rangle + \langle \overline{u_i' s'^2} \rangle\right] - \langle \epsilon_s \rangle$$
$$+ \left\langle \bar{s}'' \frac{\partial \tau_{si}''}{\partial x_i} \right\rangle + \langle \overline{s' Q_s'} \rangle. \tag{A5}$$

The first and the second terms on the r.h.s. of equation (A5) describe the mean-gradient production-destruction and the third-order transport of the SGS scalar variance, respectively. The previous last term on the r.h.s. is equal in magnitude but opposite in sign to the previous last term in equation (A2). It can be interpreted as a scale-interaction term which describes the transfer of scalar variance between the resolved and the subgrid scales [*Mironov and Sullivan*, 2010]. The scale-interaction terms cancel out if the budget of the total scalar variance $\langle \bar{s}''^2 \rangle + \langle \zeta \rangle$ is considered.

The total scalar-variance budget is obtained by adding (A2) and (A5). The result is

$$\frac{1}{2}\left(\frac{\partial}{\partial t}+\langle\bar{u}_i\rangle\frac{\partial}{\partial x_i}\right)\left(\langle\bar{s}''^2\rangle+\langle\zeta\rangle\right)=-\left(\langle\bar{u}_i''\bar{s}''\rangle+\langle\tau_{si}\rangle\right)\frac{\partial\langle\bar{s}\rangle}{\partial x_i}$$
$$-\frac{1}{2}\frac{\partial}{\partial x_i}\left[\langle\bar{u}_i''\bar{s}''^2\rangle+\langle\bar{u}_i''\zeta''\rangle+2\langle\bar{s}''\tau_{si}''\rangle+\langle\overline{u_i's'^2}\rangle\right] \tag{A6}$$
$$-\langle\epsilon_s\rangle+\langle\bar{s}''\bar{Q}_s''\rangle+\langle\overline{s'Q_s'}\rangle.$$

The time mean of equation (A6) is treated as an approximation to the ensemble-mean scalar-variance budget equation (see section 2 for details of time averaging).

Due to the cyclic lateral boundary conditions and zero horizontal-mean vertical velocity, equation (A6) is simplified to give the scalar-variance budget equation in the form

$$\frac{1}{2}\frac{\partial}{\partial t}\left(\langle\bar{s}''^2\rangle+\langle\zeta\rangle\right)=-\left(\langle\bar{u}_3''\bar{s}''\rangle+\langle\tau_{s3}\rangle\right)\frac{\partial\langle\bar{s}\rangle}{\partial x_3}$$
$$-\frac{1}{2}\frac{\partial}{\partial x_3}\left[\langle\bar{u}_3''\bar{s}''^2\rangle+\langle\bar{u}_3''\zeta''\rangle+2\langle\bar{s}''\tau_{s3}''\rangle+\langle\overline{u_3's'^2}\rangle\right] \tag{A7}$$
$$-\langle\epsilon_s\rangle+\langle\bar{s}''\bar{Q}_s''\rangle.$$

The SGS fluctuations of the scalar source are not accounted for in our simulations, hence the term $\langle\overline{s'Q_s'}\rangle$ is zero (see section 3.1).

Neither the scalar variance ζ nor its dissipation rate ϵ_s is computed by the SGS model used within PALM. An estimate of ϵ_s is obtained by assuming that production and dissipation of the scalar variance are approximately in balance and that turbulence is locally isotropic at the subgrid scales. This gives [see *Peltier and Wyngaard*, 1995, for discussion] $\epsilon_s = K_s(\partial\bar{s}/\partial x_i)^2$, where $K_s = C_K(1+2\Delta^{-1}l)le^{1/2}$ is the SGS eddy diffusivity, l is the SGS turbulence length scale (computed with due regard for the effect of static stability), $\Delta = (\Delta_1\Delta_2\Delta_3)^{1/3}$, Δ_1, Δ_2, and Δ_3 being the grid spacing in x_1, x_2, and x_3 directions, respectively, and C_K is a dimensionless constant. Similar reasoning gives an estimate of ζ. Using a down-gradient approximation for the scalar flux, $\tau_{si} = -K_s\partial\bar{s}/\partial x_i$, and an expression of the scalar-variance dissipation rate in terms of the length scale and the SGS TKE, $\epsilon_s = C_\zeta l^{-1}e^{1/2}\zeta$, C_ζ being a dimensionless constant, we obtain $\zeta = 5e^{-1}\tau_{si}^2$, where the numerical value of the coefficient is based on the scalar-variance spectrum in the inertial subrange [*Moeng and Wyngaard*, 1988]. The SGS third-order transport term $\overline{u_i's'^2}$ (the SGS flux of the SGS scalar variance) cannot be determined within the SGS model of PALM and is therefore considered as part of the budget residual. This term should be small in high-resolution LES.

One further comment is in order as to the second-moment budgets obtained on the basis of LES data. Since in both BOMEX and DYCOMS cases discussed in the present paper tendencies due to large-scale subsidence are added to the prognostic equations for the horizontal velocity components, the liquid water potential temperature and the total water specific humidity (see section 2), the terms due to large-scale subsidence should also appear in the second-moment budget equations. For example, the term $-\frac{1}{2}w_{subs}\partial\langle\bar{s}''^2\rangle/\partial x_3$, w_{subs} being the (prescribed) large-scale subsidence velocity independent of x_1 and x_2, should appear on the r.h.s. of equation (A7). The terms due to w_{subs} proved to be negligibly small in all second-moment budgets considered in the present paper.

Appendix B: Estimation of SGS Pressure-Velocity and Pressure-Scalar Covariances

As the analysis of *Khanna* [1998], M00 and *Mironov* [2001] suggest, the SGS pressure gradient-scalar covariance,

$$\mathcal{P}_{si} = -\frac{1}{\rho_0}\left\langle\overline{s'\frac{\partial p'}{\partial x_i}}\right\rangle, \tag{B1}$$

should be accounted for to close the scalar-flux budget, equation (3), to a good approximation. Ignoring $\mathcal{P}_{si}$ results in a significant budget residual, even though the resolution of LES runs may be relatively high.

An estimate of the SGS pressure gradient-scalar covariance can be obtained on the basis of the budget equation for the (horizontally) averaged SGS scalar flux $\langle\tau_{si}\rangle$ (see M00 and *Mironov* [2001], for discussion). That equation reads

$$\left(\frac{\partial}{\partial t}+\langle\bar{u}_j\rangle\frac{\partial}{\partial x_j}\right)\langle\tau_{si}\rangle=-\left\langle\tau_{sj}\frac{\partial\bar{u}_i}{\partial x_j}\right\rangle-\left\langle\tau_{ij}\frac{\partial\bar{s}}{\partial x_j}\right\rangle+\frac{g}{\theta_0}\delta_{i3}\langle\tau_{vs}\rangle-\varepsilon_{ijk}f_j\langle\tau_{sk}\rangle$$

$$-\frac{\partial}{\partial x_j}\left[\langle\bar{u}_j''\tau_{si}''\rangle+\langle\overline{u_j'u_i's'}\rangle\right]+\mathcal{P}_{si}, \tag{B2}$$

where $\tau_{vs}=\overline{s'\theta_v'}$ is the SGS virtual potential temperature-scalar covariance, and the SGS source term is not accounted for (cf. the discussion of the SGS scalar-variance budget in Appendix A). Neglecting the time-rate-of-change, advection and third-order turbulent transport terms (these are presumably small in high-resolution LES), i.e., the l.h.s. and the previous last term on the r.h.s. of equation (B2), the SGS scalar-flux equation reduces to a local balance between the mean-shear, mean-scalar-gradient, buoyancy, Coriolis, and pressure gradient-scalar covariance terms. This yields an approximation

$$\mathcal{P}_{si}=\left\langle\tau_{sj}\frac{\partial\bar{u}_i}{\partial x_j}\right\rangle+\left\langle\tau_{ij}\frac{\partial\bar{s}}{\partial x_j}\right\rangle-\delta_{i3}\frac{g}{\theta_0}\langle\tau_{vs}\rangle+\varepsilon_{ijk}f_j\langle\tau_{sk}\rangle, \tag{B3}$$

where the SGS quantities τ_{ij}, τ_{si}, and τ_{vs} are computed by the SGS model of PALM.

An estimate of the SGS pressure-strain correlation (that can also be referred to as the SGS pressure scrambling term),

$$\mathcal{P}_{ij}=\left\langle\overline{p'\left(\frac{\partial u_i'}{\partial x_j}+\frac{\partial u_j'}{\partial x_i}\right)}\right\rangle, \tag{B4}$$

can be obtained in much the same way as the estimate of $\mathcal{P}_{si}$. It must be remembered, however, that $\mathcal{P}_{ij}$ is a traceless tensor. Physically, $\mathcal{P}_{ij}$ acts to exchange energy between the Reynolds-stress tensor components but it does not affect the TKE. An approximation of $\mathcal{P}_{ij}$ is conveniently obtained on the basis of the budget equation for the SGS departure-from-isotropy tensor defined as $\tau_{ij}-\frac{2}{3}\delta_{ij}e$, $e=\frac{1}{2}\tau_{ii}$ being the SGS TKE. The equation for the departure-from-isotropy tensor is derived by subtracting the SGS TKE equation multiplied by $\frac{2}{3}\delta_{ij}$ from the equation for τ_{ij} [see *Deardorff*, 1973, equation (2.4)]. Upon (horizontal) averaging, we obtain

$$\left(\frac{\partial}{\partial t}+\langle\bar{u}_k\rangle\frac{\partial}{\partial x_k}\right)\left\langle\tau_{ij}-\frac{2}{3}\delta_{ij}e\right\rangle=-\left[\left\langle\tau_{jk}\frac{\partial\bar{u}_i}{\partial x_k}\right\rangle+\left\langle\tau_{ik}\frac{\partial\bar{u}_j}{\partial x_k}\right\rangle-\frac{2}{3}\delta_{ij}\left\langle\tau_{kl}\frac{\partial\bar{u}_k}{\partial x_l}\right\rangle\right]$$

$$+\frac{g}{\theta_0}\left[\delta_{i3}\langle\tau_{vj}\rangle+\delta_{j3}\langle\tau_{vi}\rangle-\frac{2}{3}\delta_{ij}\langle\tau_{v3}\rangle\right]$$

$$-\varepsilon_{ikl}f_k\langle\tau_{jl}\rangle-\varepsilon_{jkl}f_k\langle\tau_{il}\rangle+\mathcal{P}_{ij} \tag{B5}$$

$$-\frac{\partial}{\partial x_k}\left[\langle\bar{u}_k''\tau_{ij}''\rangle-\frac{2}{3}\delta_{ij}\langle\bar{u}_k''e''\rangle+\langle\overline{u_k'u_i'u_j'}\rangle-\frac{1}{3}\delta_{ij}\langle\overline{u_k'u_l'^2}\rangle\right]$$

$$-\frac{1}{\rho_0}\frac{\partial}{\partial x_k}\left[\delta_{jk}\langle\overline{u_i'p'}\rangle+\delta_{ik}\langle\overline{u_j'p'}\rangle-\frac{2}{3}\delta_{ij}\langle\overline{u_k'p'}\rangle\right].$$

Neglecting the time-rate-of-change and the advection terms as well as the third-order transport and the pressure transport terms, i.e., the l.h.s. and the last two terms on the r.h.s. of equation (B5), the equation for the SGS departure-from-isotropy tensor reduces to a local balance between the mean-shear, buoyancy, Coriolis, and pressure-strain correlation terms. This yields an approximation in the form

$$\mathcal{P}_{ij}=\left\langle\tau_{jk}\frac{\partial\bar{u}_i}{\partial x_k}\right\rangle+\left\langle\tau_{ik}\frac{\partial\bar{u}_j}{\partial x_k}\right\rangle-\frac{2}{3}\delta_{ij}\left\langle\tau_{kl}\frac{\partial\bar{u}_k}{\partial x_l}\right\rangle-\frac{g}{\theta_0}\left[\delta_{i3}\langle\tau_{vj}\rangle+\delta_{j3}\langle\tau_{vi}\rangle-\frac{2}{3}\delta_{ij}\langle\tau_{v3}\rangle\right]$$

$$+\varepsilon_{ikl}f_k\langle\tau_{jl}\rangle+\varepsilon_{jkl}f_k\langle\tau_{il}\rangle. \tag{B6}$$

References

Andreas, E. L. (1987), On the Kolmogorov constants for the temperature-humidity cospectrum and the refractive index spectrum, *J. Atmos. Sci.*, *44*, 2399–2406, doi:10.1175/1520-0469(1987)044<2399:OTKCFT>2.0.CO;2.

Brost, R. A., J. C. Wyngaard, and D. H. Lenschow (1982), Marine stratocumulus layers. Part II: Turbulence budgets, *J. Atmos. Sci.*, *39*, 818–836, doi:10.1175/1520-0469(1982)039<0818:MSLPIT>2.0.CO;2.

Brown, A. R. (1999), Large-eddy simulation and parameterization of the effects of shear on shallow cumulus convection, *Boundary Layer Meteorol.*, *91*, 65–80, doi:10.1023/A:1001836612775.

Chlond, A., and A. Wolkau (2000), Large-eddy simulation of a nocturnal stratocumulus-topped marine atmospheric boundary layer: An uncertainty analysis, *Boundary Layer Meteorol.*, *95*, 31–55, doi:10.1023/A:1002438701638.

Conzemius, R. J., and E. Fedorovich (2006), Dynamics of sheared convective boundary layer entrainment. Part I: Methodological background and large-eddy simulations, *J. Atmos. Sci.*, *63*, 1151–1178, doi:10.1175/JAS3691.1.

Cuijpers, J. W. M., and P. G. Duynkerke (1993), Large eddy simulation of trade wind cumulus clouds, *J. Atmos. Sci.*, *50*, 3894–3908, doi:10.1175/1520-0469(1993)050<3894:LESOTW>2.0.CO;2.

Cuijpers, J. W. M., P. G. Duynkerke, and F. T. M. Nieuwstadt (1996), Analyses of variance and flux budgets in cumulus-topped boundary layers, *Atmos. Res.*, *40*, 307–337, doi:10.1016/0169-8095(95)00033-X.

de Roode, S. R., and C. S. Bretherton (2003), Mass-flux budgets of shallow cumulus clouds, *J. Atmos. Sci.*, *60*, 137–151, doi:10.1175/1520-0469(2003)060<0137:MFBOSC>2.0.CO;2.

Deardorff, J. W. (1970), Convective velocity and temperature scales for the unstable planetary boundary layer and for Rayleigh convection, *J. Atmos. Sci.*, *27*, 1211–1213, doi:10.1175/1520-0469(1970)027<1211:CVATSF>2.0.CO;2.

Deardorff, J. W. (1973), The use of subgrid transport equations in a three-dimensional model of atmospheric turbulence, *J. Fluid Eng.*, *95*, 429–438, doi:10.1115/1.3447047.

Deardorff, J. W. (1974a), Three-dimensional numerical study of the height and mean structure of a heated planetary boundary layer, *Boundary Layer Meteorol.*, *7*, 81–106, doi:10.1007/BF00224974.

Deardorff, J. W. (1974b), Three-dimensional numerical study of turbulence in an entraining mixed layer, *Boundary Layer Meteorol.*, *7*, 199–226, doi:10.1007/BF00227913.

Deardorff, J. W. (1980), Stratocumulus-capped mixed layers derived from a three-dimensional model, *Boundary Layer Meteorol.*, *18*, 495–527, doi:10.1007/BF00119502.

Ghosal, S. (1996), An analysis of numerical errors in large-eddy simulations of turbulence, *J. Comput. Phys.*, *125*, 187–206, doi:10.1006/jcph.1996.0088.

Glendening, J. W., and T. Haack (2001), Influence of advection differencing error upon large-eddy simulation accuracy, *Boundary Layer Meteorol.*, *98*, 127–153, doi:10.1023/A:1018734205850.

Golaz, J.-C., S. Wang, J. D. Doyle, and J. M. Schmidt (2005), COAMPS-LES: Model evaluation and analysis of second-and third order moment vertical velocity budgets, *Boundary Layer Meteorol.*, *116*, 487–517, doi:10.1007/s10546-004-7300-5.

Grant, A. L. M., and A. P. Lock (2004), The turbulent kinetic energy budget for shallow cumulus convection, *Q. J. R. Meteorol. Soc.*, *130*, 401–422, doi:10.1256/qj.03.50.

Hanjalić, K., and B. Launder (2011), *Modelling Turbulence in Engineering and the Environment—Second-Moment Routes to Closures*, 379 pp., Cambridge Univ. Press, Cambridge, U. K.

Khairoutdinov, M. F., and D. A. Randall (2002), Similarity of deep continental cumulus convection as revealed by a three-dimensional cloud-resolving model, *J. Atmos. Sci.*, *59*, 2550–2566, doi:10.1175/1520-0469(2002)059<2550:SODCCC>2.0.CO;2.

Khanna, S. (1998), Comparison of Kansas data with high-resolution large-eddy simulation fields, *Boundary Layer Meteorol.*, *88*, 121–144, doi:10.1023/A:1001068612129.

Lenschow, D. H., and B. B. Stankov (1986), Length scales in the convective boundary layer, *J. Atmos. Sci.*, *43*, 1198–1209, doi:10.1175/1520-0469(1986)043<1198:LSITCB>2.0.CO;2.

Lenschow, D. H., J. C. Wyngaard, and W. T. Pennel (1980), Mean-field and second-moment budgets in a baroclinic, convective boundary layer, *J. Atmos. Sci.*, *37*, 1313–1326, doi:10.1175/1520-0469(1980)037<1313:MFASMB>2.0.CO;2.

Lilly, D. K. (1967), The representation of small-scale turbulence in numerical simulation experiments, in Proceedings of the IBM Scientific Computing Symposium Environmental Sciences, NCAR Manuscript 281, pp. 195–210, White Planes, N. Y., doi:10.5065/D62R3PMM.

Maronga, B., A. F. Moene, D. van Dinther, S. Raasch, F. Bosveld, and B. Gioli (2013), Derivation of structure parameters in the convective boundary layer from large-eddy simulations and implications for the interpretation of scintillometer observations, *Boundary Layer Meteorol.*, *148*, 1–30, doi:10.1007/s10546-013-9801-6.

Maronga, B., M. Gryschka, R. Heinze, F. Hoffmann, F. Kanani-Sühring, M. Keck, K. Ketelsen, M. O. Letzel, M. Sühring, and S. Raasch (2015), The Parallelized Large-Eddy Simulation Model (PALM) version 4.0 for Atmospheric and Oceanic Flows: Model Formulation, Recent Developments, and Future Perspectives, *Geosci. Model Dev. Discuss.*, *8*, 1539–1637, doi:10.5194/gmdd-8-1539-2015.

Mason, P. J. (1989), Large-eddy simulation of the convective atmospheric boundary layer, *J. Atmos. Sci.*, *46*, 1492–1516, doi:10.1175/1520-0469(1989)046<1492:LESOTC>2.0.CO;2.

Mironov, D. V. (2001), Pressure-potential temperature covariance in convection with rotation, *Q. J. R. Meteorol. Soc.*, *127*, 89–110, doi:10.1256/smsqj.57105.

Mironov, D. V. (2009), Turbulence in the lower troposphere: Second-order closure and mass-flux modelling frameworks, *Lect. Notes Phys.*, *756*, 161–221, doi:10.1007/978-3-540-78961-1_5.

Mironov, D. V., and P. P. Sullivan (2010), Effect of horizontal surface temperature heterogeneity on turbulent mixing in the stably stratified atmospheric boundary layer, paper 6.3 presented at 19th American Meteorological Society Symposium on Boundary Layers and Turbulence, Am. Meteorol. Soc., Keystone, Colo.

Mironov, D. V., V. M. Gryanik, C.-H. Moeng, D. J. Olbers and T. H. Warncke (2000), Vertical turbulence structure and second-moment budgets in convection with rotation: A large-eddy simulation study, *Q. J. R. Meteorol. Soc.*, *126*, 477–515, doi:10.1256/smsqj.56305.

Moeng, C.-H. (1986), Large-eddy simulation of a stratus topped boundary layer. Part I: Structure und budgets, *J. Atmos. Sci.*, *43*, 2880–2900, doi:10.1175/1520-0469(1986)043<2886:LESOAS>2.0.CO;2.

Moeng, C.-H. and J. C. Wyngaard (1988), Spectral analysis of large-eddy simulations of the convective boundary layer, *J. Atmos. Sci.*, *45*, 3573–3587, doi:10.1175/1520-0469(1988)045<3573:SAOLES>2.0.CO;2.

Moeng, C.-H., and J. C. Wyngaard (1989), Evaluation of turbulent transport and dissipation closures in second-order modeling, *J. Atmos. Sci.*, *46*, 2311–2330, doi:10.1175/1520-0469(1989)046<2311:EOTTAD>2.0.CO;2.

Morinishi, Y., T. Lund, O. Vasilyev, and P. Moin (1998), Fully conservative higher order finite difference schemes for incompressible flow, *J. Comput. Phys.*, *143*, 90–124, doi:10.1006/jcph.1998.5962.

Neggers, R. A. J. (2009), A dual mass flux framework for boundary layer convection. Part II: Clouds, *J. Atmos. Sci.*, *66*, 1489–1506, doi:10.1175/2008JAS2636.1.

Nicholls, S., and M. A. LeMone (1982), The simulation of a fair weather marine boundary layer in GATE using a three-dimensional model, *Q. J. R. Meteorol. Soc.*, *108*, 167–190, doi:10.1002/qj.49710845510.

Peltier, L. J., and J. C. Wyngaard (1995), Structure-function parameters in the convective boundary layer from large-eddy simulations, *J. Atmos. Sci.*, *52*, 3641–3660, doi:10.1175/1520-0469(1995)052<3641:SPITCB>2.0.CO;2.

Piacsek, S. A., and G. P. Williams (1970), Conservation properties of convection difference schemes, *J. Comput. Phys.*, *6*, 392–405, doi:10.1016/0021-9991(70)90038-0.

Pino, D., and J. V.-G. de Arellano (2008), Effects of shear in the convective boundary layer: Analysis of the turbulent kinetic energy budget, *Acta Geophys.*, *56*, 167–193, doi:10.2478/s11600-007-0037-z.

Pope, S. B. (2000), *Turbulent Flows*, 771 pp., Cambridge Univ. Press, Cambridge, U. K.

Raasch, S., and M. Schröter (2001), PALM—A large-eddy simulation model performing on massively parallel computers, *Meteorol. Z.*, *10*, 363–372, doi:10.1127/0941-2948/2001/0010-0363.

Riechelmann, T., Y. Noh, and S. Raasch (2012), A new method for large-eddy simulations of clouds with Lagrangian droplets including the 845 effects of turbulent collision, *New J. Phys.*, *14*, 065008, doi:10.1088/1367-2630/14/6/065008.

Schmidt, H., and U. Schumann (1989), Coherent structure of the convective boundary layer derived from large-eddy simulations, *J. Fluid Mech.*, *200*, 511–562, doi:10.1017/S0022112089000753.

Schumann, U. (1975), Subgrid scale model for finite difference simulations of turbulent flows in plane channels and annuli, *J. Comput. Phys.*, *18*, 376–404, doi:10.1016/0021-9991(75)90093-5.

Siebesma, A. P., et al. (2003), A large eddy simulation intercomparison study of shallow cumulus convection, *J. Atmos. Sci.*, *60*, 1201–1219, doi:10.1175/1520-0469(2003)60<1201:ALESIS>2.0.CO;2.

Solomon, A., M. Shupe, P. Persson, and H. Morrison (2011), Moisture and dynamical interactions maintaining decoupled Arctic mixed-phase stratocumulus in the presence of humidity inversion, *Atmos. Chem. Phys.*, *11*, 10,127–10,148, doi:10.5194/acp-11-10127-2011.

Stevens, B., et al. (2005), Evaluation of large-eddy simulations via observations of nocturnal marine stratocumlus, *Mon. Weather Rev.*, *133*, 1443–1462, doi:10.1175/MWR2930.1.

Stull, R. B. (1988), *An Introduction to Boundary Layer Meteorology*, 666 pp., Springer.

Tennekes, H., and J. L. Lumley (1972), *A First Course in Turbulence*, 300 pp., MIT Press, Cambridge, Mass.

Therry, G., and P. Lacarrere (1983), Improving the eddy kinetic energy model for planetary boundary layer description, *Boundary Layer Meteorol.*, *25*, 63–88, doi:10.1007/BF00122098.

Wicker, L. J., and W. S. Skamarock (2002), Time-splitting methods for elastic models using forward time schemes, *J. Atmos. Sci.*, *130*, 2088–2097, doi:10.1175/1520-0493(2002)130<2088:TSMFEM>2.0.CO;2.

Wyngaard, J. C. (2010), *Turbulence in the Atmosphere*, 1st ed., 393 pp., Cambridge Univ. Press, Cambridge, U. K.

Wyngaard, J. C., W. T. Pennel, D. H. Lenschow, and M. A. LeMone (1978), The temperature-humidity covariance budget in the convective boundary layer, *J. Atmos. Sci.*, *35*, 47–58, doi:10.1175/1520-0469(1978)035<0047:TTHCBI>2.0.CO;2.

Erratum